Pathophysiology of human red blood cell probed by quantitative phase microscopy

by

YongKeun Park

B.S., Seoul National University (2004)
S.M., Massachusetts Institute of Technology (2007)

Submitted to the Harvard-Massachusetts Institute of Technology
Division of Health Sciences and Technology
in Partial Fulfillment of the Requirements for the Degree of

Doctor of Philosophy

in Biomedical Engineering and Mechanical Engineering
at the
Massachusetts Institute of Technology
[June 2010]
May 2010

Signature of Author .....
Harvard-MIT Division of Health Sciences and Technology
May 24, 2010

Certified by .....
Subra Suresh
Dean of Engineering and Vannevar Bush Professor of Engineering, MIT
Thesis Supervisor

Certified by .....
Peter T. C. So
Professor of Mechanical Engineering and Biological Engineering, MIT

Certified by .....
Allard P. Mosk
Associate Professor at the MESA+ Institute for Nanotechnology, University of Twente

Certified by .....
John M. Higgins
Assistant Professor of Systems Biology, Harvard Medical School

Accepted by .....
Ram Sasisekharan
PhD/Director, Harvard-MIT Division of Health Sciences and Technology
Edward Hood Taplin Professor of Health Sciences & Technology and Biological Engineering
Chairman, Graduate Thesis Committee

Pathophysiology of human red blood cell probed by quantitative phase microscopy

by

YongKeun Park

Submitted to the Harvard-Massachusetts Institute of Technology
Division of Health Sciences and Technology on May 5, 2010 in Partial Fulfillment of
the Requirements for the degree of Doctor of Philosophy
in Biomedical Engineering and Mechanical Engineering

ABSTRACT

There is a strong correlation between the membrane fluctuations and the material properties of living cells. The former, consisting of submicron displacements, can be altered by changing the cells' pathophysiological conditions. It is our hypothesis that the material properties of cells can be retrieved when we quantify cell membrane fluctuation and combine that result with an appropriate physical model. We have developed: (1) an optical imaging technique to noninvasively quantify membrane fluctuations in red blood cells at the nanometer and millisecond scales; and (2) a model to retrieve the material properties of red blood cell membrane. The technique employs laser interferometry and provides full-field quantitative topographical information of living cells with unprecedented stability. Integration with the mathematical model provides the specific material properties from individual cell membrane fluctuations: shear modulus of the membrane; bending modulus; and viscosity of the cytoplasm. Employing these methods, we have systemically studied the material properties of human red blood cells altered by various pathophysiological conditions: morphological transition of red blood cell; parasitization by the *P. falciparum* parasites; and metabolic remodeling of the membrane driven by Adenosine-5'-triphosphate (ATP). We envision that this investigation could offer a means to link cell membrane fluctuations with the pathological conditions that lead to human disease states by quantitatively providing the alternation in material properties. A clear understanding of the mechanical alteration of red blood cells is important to studying the human diseases which cause their infection.

Research Supervisors:

Prof. Subra Suresh,

Title: Dean of Engineering, Vannevar Bush Professor of Engineering, MIT

Prof. Michael S. Feld

Title: Professor of Physics, MIT

ACKNOWLEDGEMENT

I am indebted to a great many colleagues and friends for their advice and support during my tenure at MIT. With tremendous gratitude, I acknowledge the following individuals:

The late Prof. Michael S. Feld was a great advisor and friend who patiently provided myself and my fellow students with sincere guidance and support. As a colleague, I was impressed by his amazing enthusiasm for science, and I will never forget how much I was taken care of under his leadership. I miss him badly.

Dr. Ramachandra Dasari has always shown concern and provided support well beyond necessity. Without his sincere advice, I could have not come so far.

Ever since I first met Dean Subra Suresh, his professionalism and leadership have stimulated me. Prof. Allard P. Mosk's research topics have inspired me and led me to jump into a new exciting field of research. Along with them, I thank Dr. Judith Strymish for guiding me during my clinical preceptorship. I also thank Profs. Peter So and John M. Higgins for their time and advice.

I thank all the members of the spectroscopy laboratory for the friendship and support. If I had not met Gabriel Popescu, Wonshik Choi, Kamran Badizadegan, and Christopher Fang-Yen, I could not continue to pursue this field as my career. I have great memories of working with Zahid Yaqoob, Timothy Hillman, Toyohiko Yamauchi, M. Shahrooz Amin, Niyom Lue, Seungeun Oh, Dan Fu, and Yongjin Sung. I will also miss the happy times spent with Zoya Volynskaya, Zina Queen, Ishan Barman, Obrab Scepanovic, and Jessie Weber.

Many of my happiest occasions at MIT were spent in the company of the friends I met there. In particular, the times spent with Jaewon Cha and Minyoung Ryu were always a great joy. I thank Seungeun Lee, Sunyoung Lee, Sid Chung, Yanghyo Kim, Sungmin Soon, Wonjoon Choi, JooEun Ahn, Ming-Zher Poh, Se Baek Oh, Euiheon Chung, Sangjin Ryu, DaeKeun Kim, Jinho Jang, Kwonmoo Lee, Eun Hee Kim, Jae Hyung Yi, Monica Diez, John Mills, David, J. Quinn, Hana Oh, Hyun Jin In, Hongchul Jang, Wonjae Choi, Hansohl Choi, Sungmin Kim, Yunseog Lee, Jessi Jun, Yunna Sinskey, and Taeyoon Kim for the friendship. I single out Jungmin Lee for being with me during some hard times.

Special thanks to my wife, SaeEun Choi for her unconditional love.

Every moment during my last five years at MIT was challenging, but the experience was breathtaking and precious, providing me with great joy.

TABLE OF CONTENTS

List of Figures

List of Figures

CHAPTER 1. INTRODUCTION

1.1. PARASITE INDUCED MALARIA

Malaria is a vector-borne disease caused by a protozoan parasite. Every year, it causes the death of more than 500 million people, especially young children in South Africa. *Plasmodium falciparum (P. falciparum)* and *Plasmodium vivax (P. vivax)* are the two main causes of the disease[1]. Sporozoites, parasites injected by mosquitoes, invade the tissue and then move to the liver. The receptors on sporozoites specifically bind to hepatocytes. Inside the hepatocyte, each sporozoite develops into tens of thousands of merozoites, which are released from the liver and can invade red blood cells (RBCs). After invasion of an RBC host, *P. falciparum* and *P. vivax* differentiate and multiply over two days, producing around 20 merozoites per mature parasite. Each merozoite can invade other RBCs after rupture of the parasitized RBC[2]. A key feature of the biology of *P. falciparum* is its ability to alter the material properties of infected host RBCs; they lose their deformability and adhere to the small blood vessel wall[2]. Stiffened infected RBCs fail to the splenic sinusoids, resulting in the destruction of malaria infected RBCs. The sequestered parasites cause considerable obstruction to tissue perfusion after adhesion to the lining of endothelial cells. In addition, in severe malaria there may be marked reductions in the deformability of uninfected RBCs which are exposed to but not invaded by merozoites. Individuals affected with malaria are often dehydrated and this potentially exacerbates micro-vascular obstruction by reducing perfusion pressure. The destruction of RBCs is also an inevitable part of malaria disease, and anemia further compromises oxygen delivery. During intra-erythrocytic development (48 hours after invasion of a parasite into a RBC), *P. falciparum* exports proteins that interact with the host red blood cell plasma membrane and membrane-associated spectrin network[3]. Parasite-exported proteins modify the mechanical properties of host RBCs, resulting in altered cell circulation. The *Pf*155/Ring-infected erythrocyte surface antigen (RESA), the knob associated histidine-rich protein (KAHRP), the mature parasite-infected erythrocyte surface antigen (MESA), and the *P. falciparum* erythrocyte membrane protein-1 (*Pf*EMP1) are typical proteins that alter the material properties of RBCs[4]. The detailed mechanism of those proteins is still elusive.

Most recently, the effect of RESA and KAHRP on the material properties of RBCs have been investigated by using optical tweezers[5], and micropipettes aspiration[3]. The RESA protein is discharged by the merozoite which invades the host RBC and is exported to the membrane where, once phosphorylated, it interacts with the spectrin network [5-6]. Since spectrin is crucial in the ability of RBCs to undergo deformation[7], it has been proposed that RESA could play a critical role in the modulation of the mechanical properties of a host RBC. A connection between RESA and altered *P. falciparum* infected RBC (*Pf*-RBC) mechanical properties has been demonstrated in a previous study on *Pf*-RBC membrane stability[8]. Mills et al. showed RESA causes the decrease in the deformability in ring-stage of malaria infection using optical tweezers[5]. However, the detailed role and mechanism of RESA is still not known. Adhesion is mediated by *Pf*EMP1, which can bind to host receptors including CD36 and chondroitin sulfate A (CSA)[9]. *Pf*EMP1 is concentrated on electron-dense elevations of the membrane referred to as knobs. In *Pf*-RBC, knobs appear on the membrane, which is associated with adherence to endothelial cells[10]. Knobs mainly consist of KAHRP, assembling on

the outer surface of the membrane[11]. KAHRP is required for knob formation. Current evidence suggests that the KAHRP protein interacts with various cytoskeletal components of the erythrocyte including spectrin, actin, and spectrin-actin band 4.1 complexes and these interactions may be responsible for changes in host-cell physical properties[11]. The role of KAHRP in the formation of knob and the effect to the material properties of host cells are still unknown. The investigation of these specific proteins will offer potentially new avenues for understanding the malaria parasite, which could result in new treatments for human diseases.

1.2. RED BLOOD CELL MEMBRANE

Cell membranes are essential to the life of a cell. The plasma membrane defines the cell boundary and serves as the interface between the cell and the extracellular environment [12]. Red blood cell membranes are dynamic, fluid structures (Figure 1). The lipid bilayer is a continuous double-layer arrangement of phospholipid molecules, which provides the basic structure of the membrane and serves as a relatively impermeable barrier to the passage of water-soluble molecules. Important protein molecules embedded in the lipid bilayer determines the elastic properties of the membrane. Spectrin is a 100-nm-long, peripheral membrane protein that is the major component of the cytoskeleton that underlies the RBC membrane, and accounts for its biconcave shape and its flexibility. The tail ends of spectrin tetramers are linked together to short actin filaments and other cytoskeletal proteins, integrated in a junctional complex. The spectin network thus provides elasticity to the lipid bilayer of RBCs.

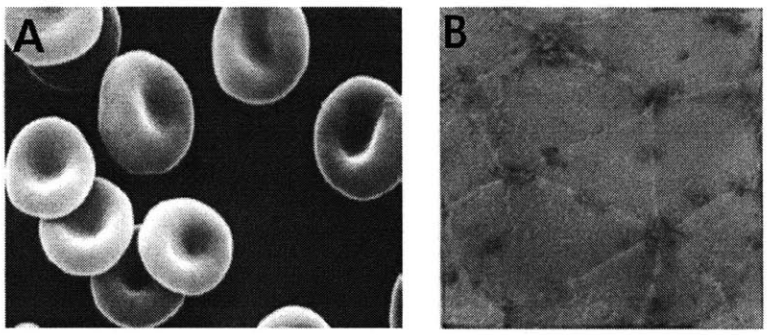

Figure 1 Scanning Electron Microscopy image of A: Red Blood Cell[13], B: membrane proteins[14].

Red blood cells must withstand large deformations during multiple passages through microvasculature and spleen sinusoids. This essential ability is diminished with senescence and disease. Cells affected by diseases such as spherocytosis, malaria, and sickle cell anemia depart from their normal discoid shape and lose their deformability [15]. Therefore, quantifying the mechanical properties of live RBCs provides insight into a variety of problems regarding the interplay of cell structure, dynamics, and function.

1.3. RED BLOOD CELL BIOPHYSICS

Pathogenesis of malaria induced by *Plasmodium falciparum* is characterized by structural and mechanical modifications to the host blood cells (RBCs). The mechanical properties of RBCs are crucial to their physiology. RBCs must withstand large mechanical deformations during repeated passages through the microvasculature and the fenestrated walls of the splenic sinusoids[16]. This essential deformability characteristic is diminished with senescence, resulting in physiological destruction of the aging RBCs. Pathological destruction of the cells occurs when they are affected by a host of diseases such as spherocytosis, or parasite-induced malaria disease, and sickle cell disease[5, 17]. Prior to their pathological destruction, RBCs depart from their normal discoid shape and lose their deformability[6, 18].

The structure of the RBC is relatively simple to model physically, compared to other biological cells, for the study of single-cell mechanics. RBCs do not have a nucleus or sub-cellular organelles and they have a well-defined biconcave shape. RBCs have a cytoskeleton cortex, which is a two-dimensional network of cross-linked elastic spectrin[19]. This spectrin network is attached to the proteins embedded into the inner surface of the cell membrane. Such a cortical cytoskeleton gives the RBC the elastic resistance to the large and repeated deformations induced when RBCs pass through the microcapillaries whose diameters are typically smaller than those of the RBCs. The phospholipid bilayer of the cell membrane is a fluid-like material which is vulnerable to lateral extension, being easily torn when extended more than 2%. RBCs have a homogeneous cytoplasm consisting mostly of hemoglobin solution[20]. The cytoplasm is fivefold more viscous than plasma, such that it provides viscous damper to absorb abrupt mechanical stress[21]. The membrane cortex consisting the lipid membrane and tethered spectrin network endows the soft and elastic properties to RBCs.

1.4. CONVENTIONAL IMAGING TECHNIQUES FOR STUDYING CELL DYNAMICS

Since Antoine van Leeuwenhoek used his home-built microscope for cell observation more than 300 years ago, optical microscopy techniques have been used in the field of biology and medicine [22]. One of the reasons why they are broadly used is an intrinsic characteristic of light – it is non-invasive and non-harmful to living cells. The transparency of cells and small organisms, however, makes cell imaging difficult because the conventional microscope, in which images are formed based on the intensity of optical wave, does not provide enough contrast enough for a transparent sample. Phase Contrast Microscopy, invented by Frits Zernike, solved this problem by converting optical phase information into intensity variations, making it easy for biologists to access and study many biological phenomena related to living cells [23]. Even though phase contrast microscopy is very commonly used to provide contrast images of a transparent live cell, it is qualitative and does not convey quantitative information about the refractive index and cell thickness.

For the past few decades, many quantitative imaging techniques have been developed for cell imaging, such as Scanning Electronic Microscopy (SEM) [24] and Atomic Force Microscopy (AFM) [25]. SEM is an electron microscopy technique which produces images by detecting electrons which are emitted from the sample surface due to excitation by the primary electron beam. SEM offers higher resolving power than optical microscopy but it requires that the samples be silver or

platinum coated prior to imaging, which is not compatible with live cell imaging. AFM is a scanning image technique with sub-nanometer resolution. When a micro-scale cantilever with a sharp tip (probe) scans the sample point by point, the laser reflected from the cantilever gives information about the height of the sample. The AFM techniques can be used on live cells, but slow point scanning limits the range of biological applications. Even though conventional quantitative imaging techniques such as SEM and AFM provide high lateral resolution, they are not well-suited for live cell imaging.

1.5. CONVENTIONAL TECHNIQUES FOR PROBING CELL MECHANICAL PROPERTIES

Various experimental techniques have been developed to investigate the mechanical behavior of live cells (Figure 2).

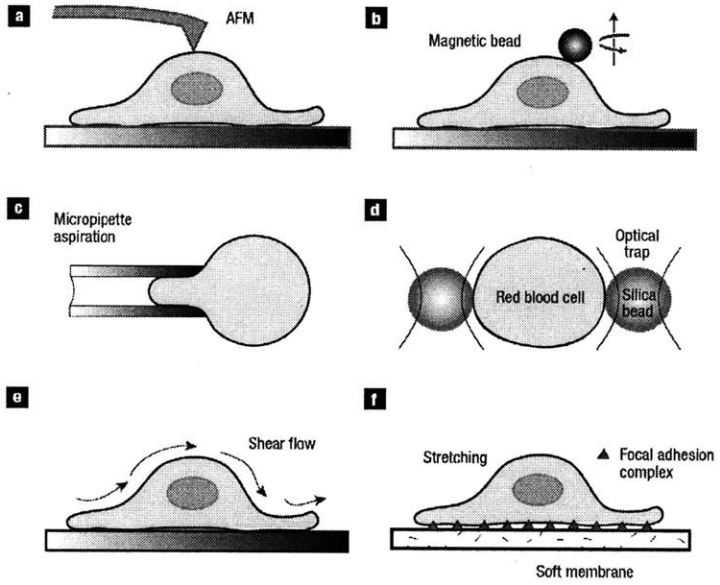

Figure 2 Conventional techniques to probe material properties of cells. (adapted from Bao et al.[26])

AFM can generate a local deformation on the cell surface[27]. The applied force can be calculated from the deflection of the cantilever tip. The effective elasticity of cell can be calculated from the applied deformation and force. In Magnetic Twisting cytometry (MTC), magnetic beads coated with functionalized surfaces are attached to the surface of a cell. An applied magnetic field imposes a twisting moment on the beads, thereby deforming a portion of the cell [28]. An appropriate analysis provides the elastic and/or viscoelastic properties of the cell[29]. In micropipette aspiration[30], a cell can be deformed by applying negative pressure through a micropipette placed on its surface. By measuring the geometry of deformed cell, the elastic response of a cell can be calculated. Optical tweezers apply an attraction force to a dielectric bead of high refractive index by a focused laser beam. They are adapted to deform a single cell[5, 17, 31]. Two micro beads (typically one to several micrometres in diameter) attached to the opposite ends of a cell, are stretched in opposite directions. The force is estimated by the input power of the laser source and a cell shape is imaged by optical microscopy to calculate the deformation. Shear-flow experiments are usually used to

study the mechanical response of a large number of cells ($N = 10^2 - 10^4$). They are conducted by either: a cone-and-plate viscometer, a rotating inverted cone to apply turbulence or laminar flows to the cell laid out on substrates; or a parallel-plate flow chamber in which cells are subjected to laminar flow[32]. In both cases the shear stress is applied to the surface of cells and deformations of cells are quantified. Elastic-membrane stretching devices have also been used to deform adherent cells[33]. Cells are cultured on a thin-sheet polymer substrate, which is coated with extra cellular matrix (ECM) molecules for cell adhesion. The substrate is then stretched while maintaining the cell's viability. In this manner, the effects of mechanical loading on cell morphology can be examined. The techniques introduced above have been widely used to investigate the mechanical properties of cells, but not all the techniques are suitable for the study of red blood cells. RBCs are 100 - 1000 times softer in elastic modulus than other cell types and they generally do not adhere to the ECM molecule, which makes it difficult to probe their material properties using AFM, shear flow, and stretching substrate, etc. Instead, the micropipette aspiration and optical tweezers techniques are typically used for studying the mechanical response of RBCs and recently MTC has been used to study their material properties[34-35].

CHAPTER 2. METHODS

2.1. DIFFRACTION PHASE MICROSCOPY[1]

In order to study dynamics of living cell membrane fluctuations, we have developed a technique called diffraction phase microscopy (DPM)[37-38]. The DPM instrument consists of an interference microscope that is incorporated into a conventional inverted fluorescence microscope. The quantitative phase images are characterized by sub-nanometer optical path-length stability over periods from milliseconds to a cell lifetime. The potential of the technique for quantifying rapid nanoscale motions in live cells can be utilized to investigate the membrane fluctuations of RBCs, while the composite phase-fluorescence imaging mode can be used to identify the presence of parasites with labels such as DAPI.

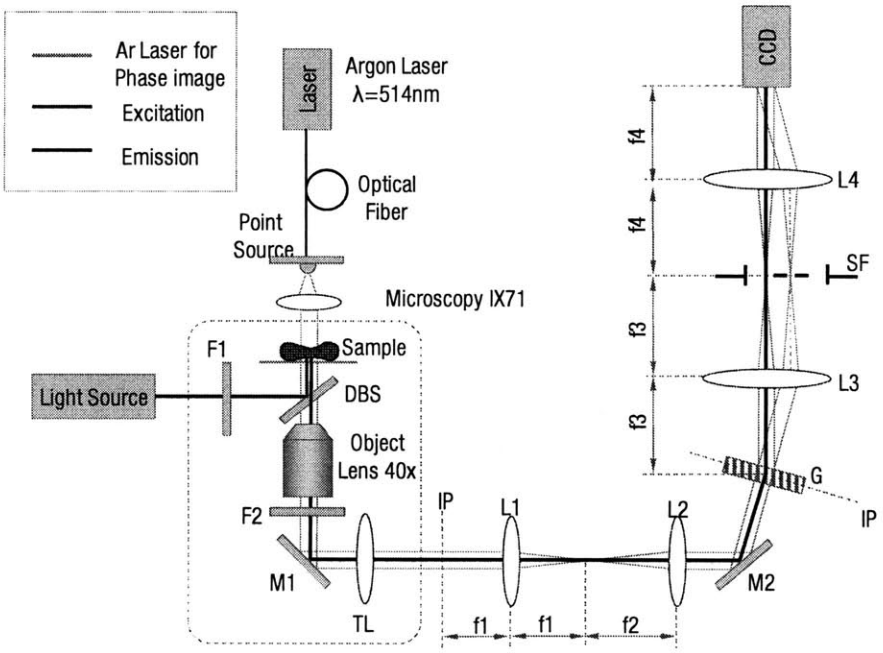

Figure 3 Illustration of DPM setup. F1, 2, filters; M1, 2, mirrors; L1-4 lenses (f1-4, respective focal lengths); G, grating; SF, spatial filter; IP1, 2, image planes; SF, spatial filter.

The DPM experimental setup is depicted in Figure 3. An inverted microscope (IX71, Olympus Inc.) is equipped for standard epi-fluorescence, using a UV lamp and an excitation-emission filter pair, F1-F2. An Ar^{2+} laser (λ = 514nm) is used as an illumination source for transmission phase imaging. Through its video output port, the microscope produces the image of the sample at the image plane IP1 with magnification M = 40×. The lens system L1-L2 is used to collimate the un-scattered field

[1] This chapter is modified from Ref. [36] with the permission from the publisher.

(spatial DC component) and further magnify the image by a factor f2/ f1=3, at the plane IP2. An amplitude grating G is placed at IP2, which generates multiple diffraction orders, each containing the full spatial information about the sample image.

The goal is to isolate the 0th and 1st orders of diffracted beams and to create a common-path Mach-Zender interferometer, with the 0th order as the reference beam and the 1st order as the sample beam. To accomplish this, a standard 4-f spatial filtering lens system L3-L4 is used. This system selects only the 0th and 1st order and generates the final interferogram at the CCD plane. The 0th order beam is low-pass filtered using a pinhole placed at the Fourier plane L3 so that it becomes a plane wave after passing through lens L4. The spatial filter passesthe entire frequency spectrum of the 1st order beam but blocks the high frequency information of the 0th beam. Unlike a conventional Mach-Zender interferometer, the two beams propagate through the same optical component, which significantly reduces the longitudinal phase noise without the need for active stabilization. The fluorescent light also passes through the grating, generating two diffraction spots in the Fourier plane of lens L3. However, due to its spatial incoherence, the fluorescence spots are much larger than the pinhole, which blocks the 0th order almost entirely. Therefore, the fluorescence image information is carried to the CCD by the 1st order of diffraction. An EMCCD camera (PhotonMAX, Princeton Instruments Inc.) is used to capture both the interferogram and the fluorescence image. The CCD has a resolution of 512×512 pixels with each pixel being 16×16 μm² in size. The grating period is 30 μm, which is smaller than the diffraction spot of the microscope at the grating plane (47μm). Thus, the optical resolution of the microscope is preserved.

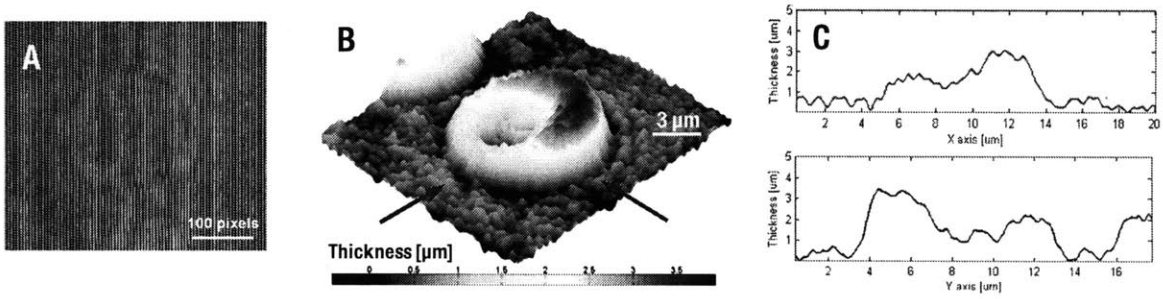

Figure 4 DPM images of single red blood cell. A. Interferogram measured by DPM B. Reconstructed topography from the interferogram in A. C. The cross section profiles of RBC topography in B.

Due to its single shot nature, the DPM technique can be applied to investigate dynamic phenomena in live cells over temporal intervals that span from the millisecond scale or less to an entire cell cycle. We demonstrate this versatility of DPM with experiments of red blood cell (RBC) membrane fluctuations, which take place at the millisecond scales. Droplets of whole blood were placed between cover slips without further preparation. Figure 4 depicts an example of such quantitative phase image of an RBC. Figure 4A shows the interferogram of single RBC measured by the CCD camera of DPM setup. From the interferogram recorded, the quantitative phase image, $\varphi(x,y,t)$ is extracted via a spatial Hilbert transform, as described elsewhere[36-37]. The instantaneous cell thickness map is obtained as $h(x,y,t)=(\lambda/2\pi\Delta n)\varphi(x,y,t)$, where λ = 514 nm is the wavelength of

the laser light used and Δn = 0.06 the refractive index contrast between the RBC and the surrounding medium as shown in Figure 4B-C. Therefore, DPM can quantitatively and non-invasively measure the membrane fluctuation in RBCs with high sensitivity and high frame rates, which can be applied to the study of *Pf*-RBCs.

2.2. TOMOGRAPHIC PHASE MICROSCOPY

Tomographic phase microscopy (TPM) is a technique developed in our laboratory, which can map the 3-D distribution of refractive index in live cells and tissues [39]. In TPM, the sample-induced optical phase shift is imaged using a phase-shifting heterodyne interferometer, as shown in Figure 5. Phase images are recorded by varying the directions of illumination. The angle of illumination ranges from -60 to 60 degree and angular step is 0.2 degree. It takes about 10 seconds to scan the entire angular range. Phase image at each step of angle corresponds to angular projection of refractive index at the illumination angle. The custom built microscopy and CMOS camera (FASTCAM 1024 PCI, Photron, Inc.) were used to measure interferograms. With the set of angular projection phase images, a filtered back-projection algorithm is used to calculate a 3D refractive index. The transverse and axial resolutions are 0.3 and 0.6 μm, respectively, and the accuracy of index measurement is 0.001.

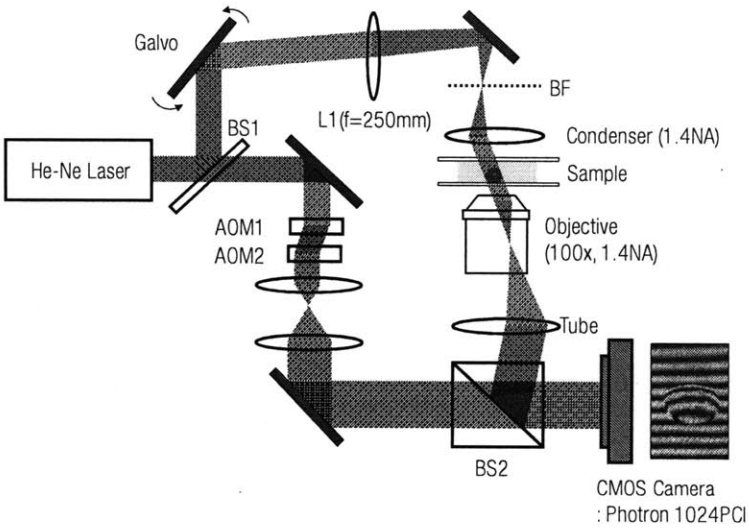

Figure 5 Tomographic phase microscope. BS1 and BS2, beamsplitters; GM, galvanometer scanning mirror; L1, focal length f = 250 mm lens; BF, back focal plane of condenser lens; L2, f =200 mm lens. The sample laser beam with original laser frequency is shown in red, and the frequency-shifted reference laser beam is shown in blue. A typical fringe pattern for a tilted beam illuminating a single HeLa cell is shown. (figure is adapted from Ref. [39])

2.3. SPECTROSCOPIC PHASE MICROSCOPY[2]

Biochemical activity of molecules governs cellular metabolism, which makes molecular concentrations important indicators of patho-physiological states of cells or tissues. Staining agents such as fluorescent dye and fluorescent protein have been widely used to quantify molecules of interest. However, the quantification of molecules using such techniques requires careful consideration on the artifacts of the staining agents: photo-bleaching; interference with metabolic activities of living cells; and non-uniform binding to the target molecules.

Refractive index (RI) can provide molecular concentration without such artifacts. As is well known, RI is related to the concentration of cellular dry mass [41]. Quantitative phase microscopy (QPM) has proven to be a useful tool to measure the phase delay induced by a specimen, which is related to its RI [37, 42-47]. However, two limitations prevent it from retrieving specific molecular concentrations from the phase delay measurements. First, the measured phase delay depends on approximate total protein contents, not the concentration [41, 48]. The phase delay is an integrated RI over the cell volume, and the RI should be decoupled from thickness to obtain molecular concentration. Second, both the phase and RI are not specific enough to differentiate single molecular species from mixtures. All types of molecules present in the cell can contribute to the RI. We note that the wavelength-dependent RI, obtained via dispersion, can resolve both limitations simultaneously. Many types of molecules can be differentiated by their dispersion. For example, Hb has significant dispersion in the visible wavelengths. Dispersion was previously used to decouple RI from thickness of cells from the dispersion of a fluorescent medium [46], and to measure the concentration of molecules in solution and in tissue sections [49].

This chapter presents a new technique, spectroscopic phase microscopy (SPM), which can measure the concentration of specific molecules in living cells and their volumes at the same time. SPM integrates diffraction phase microscopy (DPM) [36-37] and a white-light source with various bandpass filters to select various wavelengths. We demonstrate the simultaneous extraction of Hb concentration and cell volume of intact individual RBCs. Abnormalities in Hb concentration are associated with various RBC diseases (sickle-cell anemia, thalassemia, and malaria infection) [45], and the present technique will potentially lead to assessing these disease conditions quantitatively.

---

[2] This chapter is modified from Ref.[40] with the publisher's permission.

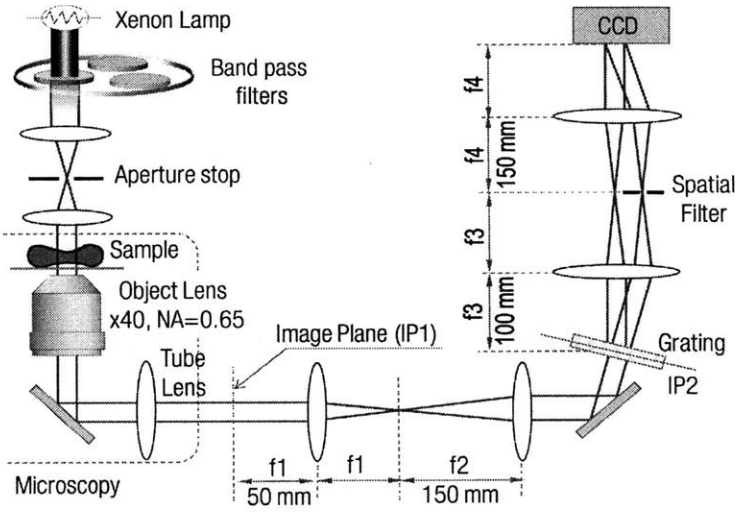

Figure 6 Experimental setup for SPM

The experimental setup consists of two parts: a white-light source with color filters for wavelength selection, and DPM for measuring quantitative phase delay (Figure 6). DPM provides highly stable phase measurements, while the use of color filters simplifies the experimental setup in switching wavelength of the light source. In dispersion measurements, a wide range of wavelengths is necessary. Either a tunable laser or a set of different lasers can be used, either of which is costly. Instead, we used a Xenon arc lamp with a set of bandpass filters. Seven different filters are used to select various center wavelengths: 440±20 nm, 546±10 nm, 560±20 nm, 580±25 nm, 600±20 nm, 655±20 nm, and 700±20 nm. The common-path geometry of DPM matches the optical path lengths for the sample and reference arms such that the alignment is independent of the wavelength and temporal coherence of the illumination source. However, it still requires high spatial coherence, due to a spatial filtering process to be described. Thus, the size of aperture stop was minimized to in order to achieve this. The E-field was extracted from the recorded interferogram by spatial Hilbert transform [37]. The grating period, 30 μm, was set to be smaller than the diffraction-limited spot of the microscopic imaging system at the grating plane. All the lenses were achromatic to minimize their contribution to chromatic dispersion.

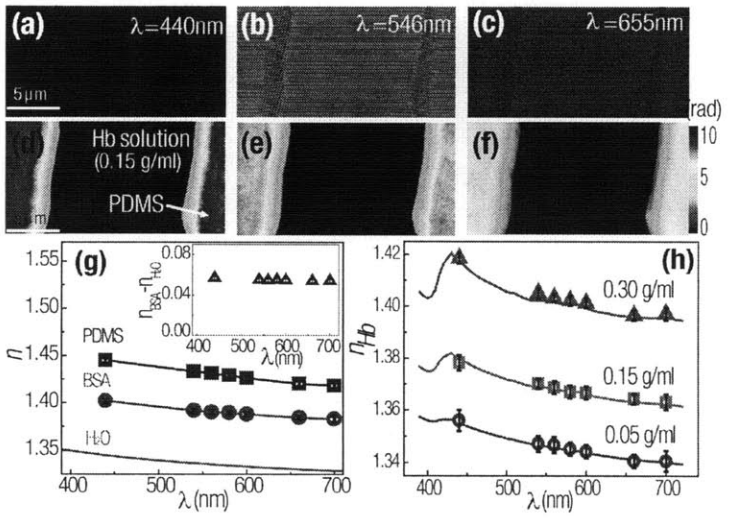

Figure 7 (a-c) Interferograms of PDMS channel filled with Hb solution. (d-f) Corresponding quantitative phase maps (g) RIs of PDMS, BSA, and water. RIs of water are adopted from Ref. [50]. *Inset*, the RI difference between BSA solution and water. (h) Measured dispersion of Hb solutions (symbols) and comparison with Ref. [51] (lines). Error bars indicate standard deviations.

To assess the ability of SPM, we measured the RIs of polydimethylsiloxane (PDMS), Bovine serum albumin (BSA), and Hb solutions at various wavelengths. Since the phase image presents the relative phase delay between a sample and a medium, a phase reference is required to determine absolute phase change induced by a specimen. We used a micro-fluidic channel and the RI of water for this purpose. We filled the PDMS channel with distilled water, and measured quantitative phase images at different wavelengths. The relative phase delay between PDMS and water is given by $\Delta\varphi = 2\pi / \lambda(n_{PDMS}(\lambda) - n_w(\lambda))h$, where λ, h, n_{PDMS} and n_w are the wavelength of the light, channel height, RI of PDMS, and RI of water, respectively. Given the known dispersion of water [50] and h = 10 μm, we obtained n_{PDMS} (Figure 7). Next, we measured the RI of the BSA solution. The measured dispersion of PDMS served as reference this time. The PDMS channel was filled with BSA solution (300 mg/ml; Gibco). From the relative phase to PDMS, the dispersion of BSA solutions were acquired using the relation, $\Delta\varphi = 2\pi(n_{PDMS}(\lambda) - n_{BSA}(\lambda;C))h/\lambda$, where $n_{BSA}(\lambda;C)$ is the RI of BSA solution at wavelength λ and concentration C. The obtained n_{BSA} is consistent with the literature [52]. Next, we measured the dispersion of Hb solutions, prepared from Hb protein powder (H7379, Sigma-Aldrich, Inc.), at three different concentrations: 0.05, 0.15, and 0.30 g/ml, respectively (Figure 7a-f). Using the method above, we obtained $n_{Hb}(\lambda;C)$ (Figure 7h), which is consistent with that of the literature [51]. From this measurement, we retrieved a linear relationship between the RI of Hb solution and its concentration at various wavelengths [41]: $n_{Hb}(\lambda;C) = \alpha(\lambda)C + n_w$, with $\alpha(\lambda)$ a specific RI increment for Hb: $\alpha(440)$ = 0.240±0.007 ml/g, $\alpha(560)$ = 0.227±0.004 ml/g, and $\alpha(660)$ = 0.221±0.005 ml/g. The albumin protein in BSA solution does not show significant dispersion in the visible range (*inset*, Figure 7g); $\alpha(\lambda)$ is 0.183 ± 0.003 ml/g for the wavelength range of 440 - 700 nm.

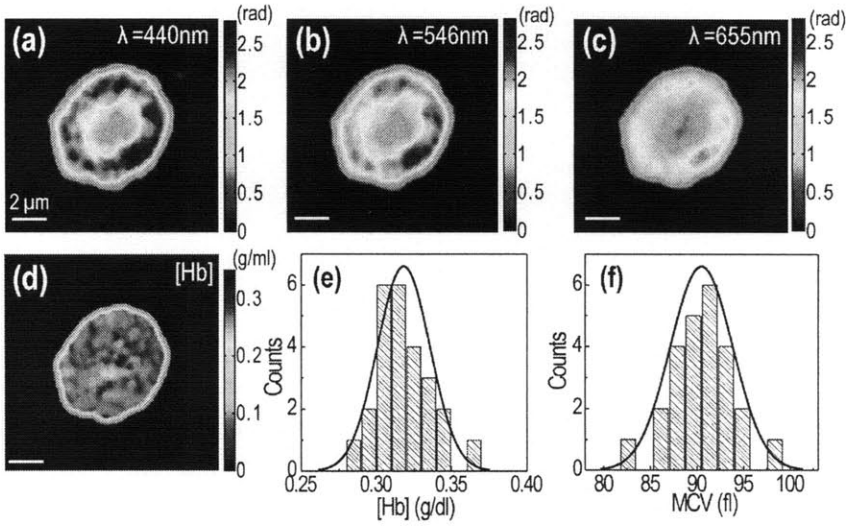

Figure 8 (a-c) Quantitative phase maps of a RBC at three different wavelengths. (d) The retrieved Hb concentration. (e) Histogram of Hb concentrations and (f) cell volumes (N=25).

Next, using the calibrated dispersion of Hb solution we applied SPM to measure cytoplasmic Hb concentration in live human RBCs. Fresh blood (5 ml) obtained by venipuncture were diluted in Phosphate-Buffered Saline (PBS) solution, and then washed three times to remove white blood cells and platelets. The interference images of RBCs were measured at the seven wavelengths (Figure 8a-c). The phase images of a RBC can be expressed as, $\Delta\varphi(x,y;\lambda) = 2\pi\left(\alpha(\lambda)C(x,y) + n_X(x,y,\lambda)\right)h(x,y)/\lambda$, with *h(x,y)* the local thickness of the cell and $n_X(x,y,\lambda)$ an relative averaged RI of other molecules besides Hb in RBC compared to water (non-Hb proteins (2.5 % of total protein mass) and ionic molecules in cytosolic space [53]). These non-Hb molecules usually do not have distinct dispersion at visible wavelengths. For example, albumin, most abundant plasma protein in mammals, has almost the same trend in RI as water in the wavelength range 440 - 700 nm (*inset*, Figure 7g). Thus, we can approximate $n_X(x,y,\lambda)$ as an independent constant of wavelength, n_X. Since $\alpha(\lambda)$ was calibrated above, there are three unknowns: *C*, n_X, and *h(x,y)*. Thus, the phase measurements at three different wavelengths are sufficient to extract *C*, n_X, and *h(x,y)* simultaneously. In principle, we can distinguish *N* different molecular contents with *N+2* spectroscopic phase measurements, assuming that they have distinctive dispersion characteristics. Figure 8d shows the retrieved Hb concentration, *C(x,y)* of a RBC. Figure 8e is a histogram of the Hb concentration in RBCs (*N* = 25). The average value is 0.318±1.7 g/ml. From the measured area of the cells and corresponding thickness, we calculated the cell volume (Figure 8f). The average value is 90.5±3.3 fl. These results are within normal physiological range [53]. According to the measured conversion factors, the sensitivity of SPM is 0.0009-0.0014 g/ml for Hb concentration, since the sensitivity in phase measurement of DPM is ~3 mrad [36]. This sensitivity corresponds to 0.08-0.13 pl for Hb contents per cell, assuming the average red blood cell volume is 90 fl.

Taken together, we have presented SPM, a simple and practical method for spectroscopic phase imaging, which can simultaneously measure Hb concentrations and cell volume of living RBCs. This new instrument has many potential applications, one of which we give here, quantifying isomeric shifts in Hb (oxy- and deoxy-Hb) when exposed to different oxygen pressures. Binding of oxygen to Hb proteins cause conformational changes which result in significant differences in dispersion. Thus, the SPM instrument may provide a valuable tool for better understanding of oxygen transport by RBCs.

2.4. MATHEMATICAL MODEL TO RETRIEVE MECHANICAL PROPERTIES[3]

The standard description of a RBC treats the membrane as a flat surface; in reality the membrane of a RBC is curved and has the compact topology of a sphere. In our theoretical analysis we simplify the complex shape of a RBC to that of a sphere to produce an analytically tractable model of membrane elasticity and fluid hydrodynamics that still incorporates the effects of the curvature and topology of a RBC. Because of that curvature, the bending and compression modes of a spherical membrane are coupled in the linear order in deformations. In order to understand the thermally generated height fluctuation spectrum of a spherical membrane, we need to account for the full linear response of the membrane to applied (radial) forces; due to the geometric coupling of bending and compression at linear order we are obliged to study both deformation modes. The geometric coupling of bending and compression generates undulatory dynamics consistent with the experiments, and does not require the postulation of a surface-tension-like term in the Hamiltonian of the composite membrane [55]. The bending and compression modes of a flat membrane are linearly independent. Thus, when the wavelength of the RBC undulations is small compared to its radius, these modes become approximately decoupled into a bending mode – which we refer to as the Lennon-Brochard (LB) mode – and a compression (C) mode. We then calculate the height-height correlation function of the RBC, which is the experimental quantity used to probe its undulatory dynamics. In addition, we map the ellipsoidal shape of the discocyte and echinocyte RBCs onto our theoretical spherical model.

The deformation energy of the spherical membrane includes a bending energy F_b and an in-plane elastic energy F_e. To understand the thermal fluctuations of the membrane, an energy quadratic in the deformations is sufficient. These energies take the well-known Helfrich form[3,4]

$$F_b = \frac{\kappa}{2}\int d^2 s (K_\alpha^\alpha - c_0)^2 , \tag{1}$$

$$F_e = \int d^2 s \left[\mu E_\alpha^\beta E_\beta^\alpha + \frac{\lambda}{2}\left(E_\alpha^\alpha\right)^2 \right], \tag{2}$$

---

[3] This chapter is modified from Ref.[54] with the publisher's permission.

where d^2s is an element of area on the surface, κ is the bending modulus, K_α^α is the trace of the curvature tensor, λ and μ are the two 2D Lamé coefficients required to describe the elasticity of the isotropic composite (i.e. lipid and spectrin) membrane, and E_β^α is a two-dimensional (2D) covariant strain tensor. The Greek indices run over the two (angular) coordinates of the undeformed sphere. We expect the bending modulus κ to be dominated by the elastic response of lipid membrane to curvature. The two Lamé constants, in general, describe the viscoelastic response of the composite membrane to in-plane deformation. In the frequency domain these are then complex quantities where the imaginary parts reflect the viscous or dissipative response to stress, primarily due to the lipid membrane (of viscosity η_m). Recent membrane diffusion experiments [56] and coarse grain simulations [57] have found an upper bound for the membrane viscosity of $\eta_m = 5\times10^{-3}$ μNs/m at room temperature. Since the elastic modulus of the spectrin network is on the order of 5 μN/m, the viscous (imaginary) part contribution to the shear response, $-i\omega\eta_m$, is subdominant up to frequencies of approximately 10^3 Hz. Accordingly, we fit our data using a purely elastic response to in-plane shear and compression.

The deformation vector of the material elements in the membrane can be written as $\varepsilon_\alpha = w\hat{r}_\alpha + \mathbf{t}_\alpha$, where w is the radial (i.e. out-of-plane) deformation field, $\hat{r}_\alpha$ is the unit normal of the sphere, and $\mathbf{t}_\alpha$ is the in-plane displacement vector. Since the in-plane shear deformations of the membrane do not couple to the out-of-plane deformations, we ignore shear deformations throughout this calculation. Therefore $\mathbf{t}_\alpha$ contains only compression modes, so it can be written as the gradient of a scalar: $t_\alpha = D_\alpha\Psi$. Using Eqs. (1) and (2), we can write the deformation free energy of the sphere in terms of the fields w, Ψ:

$$F_{el} = \int d^2s\left\{\frac{\kappa}{2}w\left(\Delta_\perp + \frac{2}{R^2}\right)^2 w + \frac{2K}{R}w(w+\Delta\Psi) + \frac{1}{2}(K+\mu)(\Delta_\perp\Psi)^2 + \frac{\mu}{R^2}\Psi\Delta_\perp\Psi\right\} \qquad (3)$$

where $\Delta_\perp$ is the two-dimensional in-plane Laplacian and $K=\mu+\lambda$. To investigate the undulatory dynamics of the membrane, we also need to consider the coupling of the bulk fluid flows inside and outside the sphere to the deformations of its surface. The hydrodynamics of these fluids can be described using the incompressible Stokes equation (i.e. zero Reynolds number) [58]. We allow for a difference between the interior cytosol viscosity η_c and the exterior solvent viscosity η_s. The coupling of the fluid to the membrane is done using the usual stick boundary conditions and the stress balance condition at the surface of the membrane.

We now look for the overdamped normal modes of the combined fluid/membrane system. Because of the spherical geometry of the membrane, the natural basis for the radial w and compression Ψ fields is the spherical harmonics $Y_{lm}(\theta,\phi)$. However, due to the rotational symmetry of the problem, the normal modes are independent of the azimuthal number m. For each order l, the two normal modes are solutions of the two-by-two matrix equation

$$\begin{bmatrix} w \\ \Psi \end{bmatrix} = \chi(l,m) \cdot \begin{bmatrix} f_w \\ f_\Psi \end{bmatrix} \tag{4}$$

where f_w and f_Ψ are the forces acting on the radial and compression fields of the membrane directly. The response matrix χ depends on all the elastic constants of the material, the viscosities of the interior and exterior fluids, the radius of curvature, the order l of the spherical harmonic, and the frequency ω. From the eigenvalues of this matrix we derive the decay rates of each normal mode [58]. We can relate the order of the spherical harmonic to an in-plane wave number q, via $l=qR$.

2.5. PROBING UNDULATORY DYNAMICS OF RBC MEMBRANES[4]

To quantitatively investigate the material properties of RBCs during morphological changes, we analyze the spatial and temporal correlations of the out-of-plane fluctuations of the RBC membrane and interpret them using a new viscoelastic continuum model of the composite spectrin-network/lipid membrane. This model accounts for the linear coupling between the bending and compression modes of a curved membrane, and thus provides a better description of the dynamics of the RBC than theories based on a flat membrane. The undulatory dynamics of a RBC are typically probed experimentally by measuring the spatial and temporal correlations of the out-of-plane fluctuations of the membrane. Theoretically, these correlations can be calculated using the response matrix χ defined above and the fluctuation-dissipation theorem [59]. The correlation of height fluctuations at two points on the membrane separated by the projected distance d and time t is defined by

$$C(d,t) = \langle \Delta h(d,t) \Delta h(0,0) \rangle, \tag{5}$$

where the angular brackets denote both spatial and temporal averaging. From the results of our previous work[58] and the fluctuation-dissipation theorem, we find that the Fourier transform of this function in the frequency domain is given by

$$\tilde{C}'(\gamma,\omega) = \frac{2k_B T}{\omega} \sum_{\ell>0} \mathrm{Im}[\chi_{ww}(\ell,\omega)] P_\ell(\cos\gamma), \tag{6}$$

Where $P_l(x)$ is the Legendre polynomial of l^{th} order. The experiments do not measure the radial deformations ω of the membrane directly. Rather, the experiments measure the *height* of the membrane, i.e. the projection of the radial deformations onto the z-axis. Furthermore, the height-height correlation function $\tilde{C}(d,\omega)$ is measured as a function of the projection of the distance between two points on the membrane onto the xy-plane, d. If we choose, for simplicity, the two points to lie symmetrically about the north pole of the sphere, then

---

[4] This chapter is modified from Ref.[54] with the publisher's permission.

$$\tilde{C}(d,\omega)=\left(1-\frac{d^2}{4R^2}\right)\tilde{C}'\left(\gamma=1-\frac{d^2}{2R^2},\omega\right). \tag{7}$$

we show the frequency dependence of the autocorrelation function $\tilde{C}(\gamma=0,\omega)$ in Figure 9C and the spatial decay of correlations at two fixed frequencies in Figure 9D. Figure 9C shows the transition of the autocorrelation function from an elastically dominated plateau at low frequencies to a viscously dominated region at high frequencies. In Figure 9d we show the spatial decay of the height-height correlations at two fixed frequencies: one corresponding to the elastic plateau (low frequency, blue curve) and one to the viscously-dominated regime (high frequency, red curve). At lower frequencies, we see a pronounced oscillatory behavior in the correlation function. The negative correlations are due to the dominance of the small-*l* contributions to the response function at low frequencies. At higher frequencies, we see that there is a shorter-ranged and nearly monotonic decay of the height-height correlations.

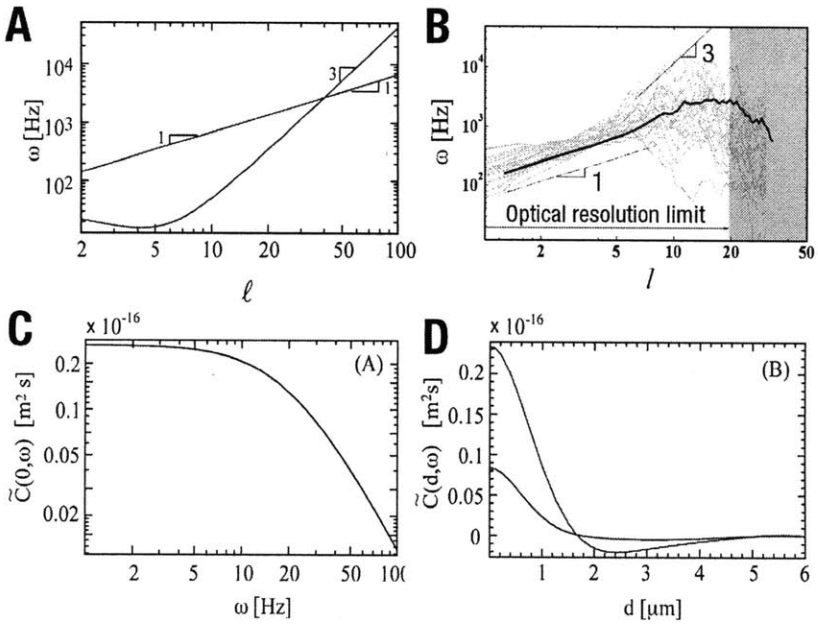

Figure 9 Computed membrane undulation. A, Decay rates for the LB mode ω_ℓ^{LB} (blue line) and the C mode ω_ℓ^{C} (red line) as a function of the order of the spherical harmonic $\ell \geq 1$ for a spherical shell with $\kappa = 20\times k_B T, R = 3\mu m$, η_s=10^{-3} $Pa\cdot s$, η_c=5×10^{-3} $Pa\cdot s$,and μ=λ=5 $\mu N/m$. B, decay rates measured from DCs (faint lines, N=30) and the averaged data (think line) C, height-height autocorrelation function as a function of the frequency, for the parameter values listed above. D, correlation function as a function of the projected distance *d* for 5 rad/sec (blue line) and 50 rad/sec (red line), for the parameter values listed above. Remarkably, this mode coupling predicts a decay rate $\omega \propto q$, which is identical to the behavior by a model of the membrane with an effective surface tension proposed by Gov et al.[55, 60]. In order to address this effect of curvature in an analytically tractable manner, we simplify the geometry of the RBC to that of a sphere.

In this chapter, we presented the physical model of dynamic fluctuations in red blood cell membrane cortex. By comparing the cross correlation functions derived from this physical model with ones measured from experiments, we can retrieve the mechanical properties of RBC membrane. We will present the results in the following chapters.

CHAPTER 3. RBC MECHANICS PART I: PHYSIOLOGICAL EFFECTS

3.1. MORPHOLOGICAL EFFECTS[5]

In this section we communicate new measurements of RBC mechanics that rely on novel experimental and theoretical techniques to characterize the mechanics and rheology of normal and pathological RBCs over a variety of length and time scales. Lacking a traditional 3D cytoskeleton, RBCs maintain their shape and mechanical integrity through a spectrin-dominated, triangular 2D network associated with the cytosolic side of their plasma membrane. This semiflexible filament network confers shear and bulk moduli to the composite membrane structure[61]. The fluid lipid bilayer is thought to be the principal contributor to the bending or curvature modulus of the composite membrane. Little is known about the molecular and structural transformations that take place in the membrane and spectrin network during the cell's morphological transitions from discocyte (DC, normal shape) to echinocyte (EC, spiculated shape) to spherocyte (SC, nearly spherical), which are accompanied by changes in RBC mechanics.

A number of techniques have been used recently to study the rheology of live cells[26]. Pipette aspiration[30], electric field deformation[62], and optical tweezers[26] provide quantitative information about the shear and bending moduli of RBC membranes in *static* conditions. However, *dynamic*, frequency-dependent knowledge of RBC mechanics is currently very limited[34]. RBC thermal fluctuations ("flickering") have been studied for more than a century[63] to better understand the interaction between the lipid bilayer and the cytoskeleton[36, 55, 64-65]. Nevertheless, quantifying these motions is experimentally challenging, and reliable spatial and temporal data are currently desirable [64, 66-67].

3.1.1. TOPOGRAPHIES OF RBCS UNDER DIFFERENT MORPHOLOGIES

We use diffraction phase microscopy (DPM)[36-37] to study the dynamics of RBCs over the commonly occurring DC-EC-SC shape transition. DPM is a highly sensitive optical imaging technique that quantifies the flickering of RBC membranes with nanometer accuracy. From measurements of dynamic fluctuations on RBC membranes, we extract the mechanical properties of the composite membrane structure. DPM provides quantitative high-stability maps of the optical paths across the living cells (Figure 10A-C). This optical path-length information can be readily translated into cell thickness, since mature RBCs, lacking nuclei and other internal structures, are characterized by a spatially uniform refractive index.

---

[5] This chapter is modified from Ref.[54] with the publisher's permission.

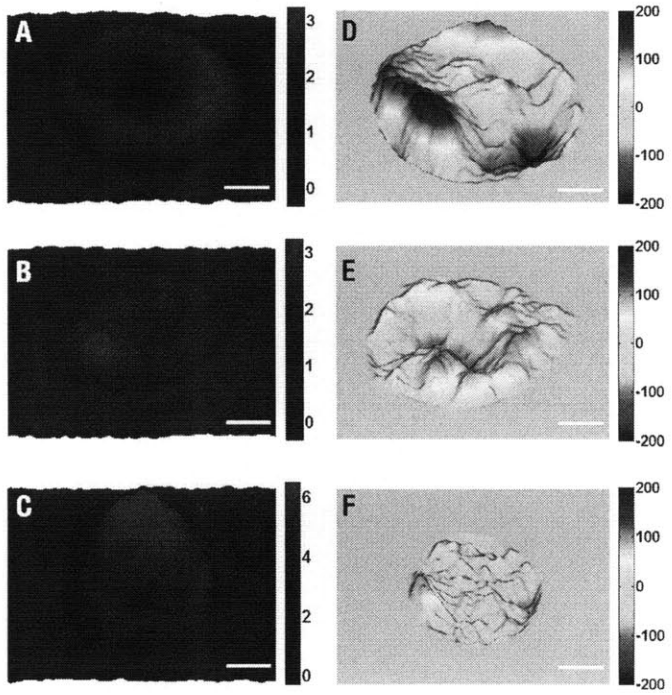

Figure 10 Red blood cells (RBCs) in three different morphologies (A-C) and instant displacement map (D-F). A, Typical RBC physical maps for discocyte (DC), B, echinocyte (EC), and C, spherocyte (SC) obtained by DPM (colorbar represents thickness in μm). D-F, Respective instantaneous displacement maps (colorbar in nm). The scale bar is 1.5 μm.

Over the morphological transition from DC to SC, the root-mean-squared amplitude of equilibrium membrane height fluctuations $\sqrt{\langle \Delta h^2 \rangle}$ decreases progressively from 46 nm (DCs) to 34 nm (ECs) and 15 nm (SCs), indicating an increasing cell stiffness (Figure 10D-F). Similarly, the long wavelength undulations observable from the instantaneous displacement map of discocytes are extinguished in spherocytes, which is another manifestation of the loss of deformability.

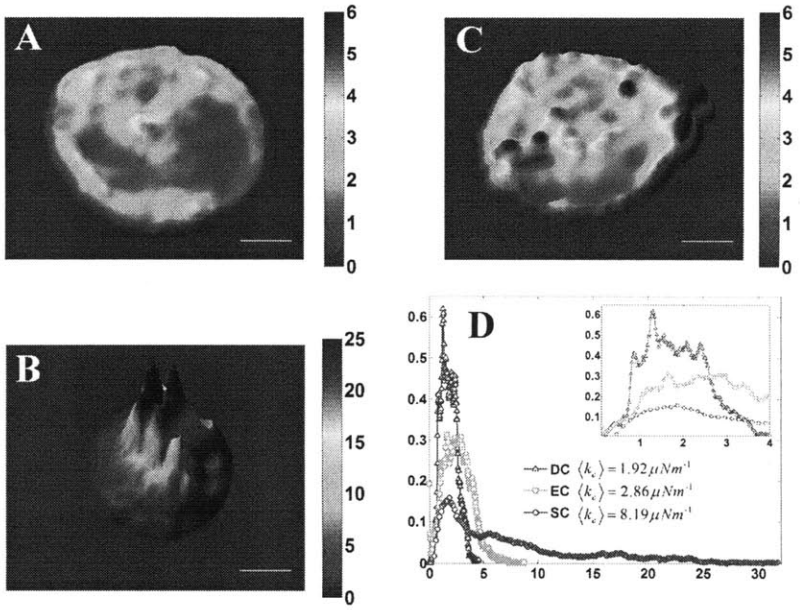

Figure 11 The effective spring constant (k_e). A-C, Typical effective spring constant map for DC (A), EC (B), and SC (C). Color bars are in μNm^{-1} and the scale bar is 1.5 μm. D, Corresponding histograms of the effective spring constant. The legend shows the respective mean values $\langle k_e \rangle$. The inset details the $\langle k_e \rangle$ behavior in the vicinity of the origin.

To characterize the time-averaged (static) behavior of the membrane elasticity, we map the cells in terms of an effective local spring constant k_e, defined by: $k_e = k_B T / \langle \Delta h^2 \rangle$ (Figure 11A-C). Examining the resulting k_e maps reveals quenched material inhomogeneities, particularly in ECs and SCs. For normal cells (DC) the central "dimple" appears to be stiffer, as shown in Figure 11A. This feature of the spatial distribution of k_e is due to a combination of local variations in the curvature and the structural properties of that part of the underlying spectrin network. We found that the extracted parameters are not highly sensitive to the more highly curved region making up the dimple. When such spatial heterogeneities are averaged over, we find that SCs are characterized by an elastic constant 4 times larger than that of DCs (Figure 11D). The average elastic constant measured for DCs, k_e = 1.9μN/m, is a factor of 3.5-10 lower than what was measured by micropipette aspiration[16] and electric field deformation[62]. This difference can be explained by noting that these two techniques probe larger cell deformations ($\Delta h \geq 1$ μm) than our technique, which measures the much smaller thermally generated membrane displacements ($3 \text{ nm} \leq |\Delta h| \leq 200 \text{ nm}$) in the absence of external stress, and thus explores the *linear* response regime.

3.1.2. MECHANICAL PROPERTIES OF RBCS UNDER DIFFERENT MORPHOLOGIES

In order to extract the material properties of the RBC, we fit our theory to the measured correlation function $\tilde{C}(d,\omega)$ by adjusting the following parameters: the shear μ and bulk $K=\mu+\lambda$ moduli of the spectrin network, the bending modulus κ of the lipid bilayer, the viscosities of the cytosol η_c and the surrounding solvent η_s, and the radius of the sphere *R*. We constrain our fits by setting *R* to the average radius of curvature of the RBC obtained directly from the data and fixing the viscosities for all data sets to be $\eta_s = 1.2$ mPa·s, $\eta_c = 5.5$ mPa·s[68-69]. Finally, for a triangular elastic network we expect $\mu = \lambda$ so we set $K = 2\mu$[70]. The fitting parameter space is now reduced to two dimensions and spanned by the bending modulus κ of the lipid bilayer and the shear modulus μ of the spectrin network. These are obtained by fitting the correlation data for each RBC.

Using DPM, we measure the height correlations versus the projected distance *d* at various frequencies ω for the three different morphological groups (Figure 12A-C). At low frequencies, we observe oscillations in the correlation function at distances of a few microns in the case of the more elastically compliant DC and EC cells. At higher frequencies, these anti-correlations are suppressed, as expected in the more viscously-dominated regime. The experimental data (thin lines) and the best fit of the average data (thick lines) are shown in Figure 12A-C. As can be seen, the theory generates a very good fit to the data including at low frequencies, where anti-correlatated motion is observed in DCs and ECs. Both at higher frequencies (red curves) and for stiffer membranes (e.g. SC cells) these anti-correlations are strongly suppressed.

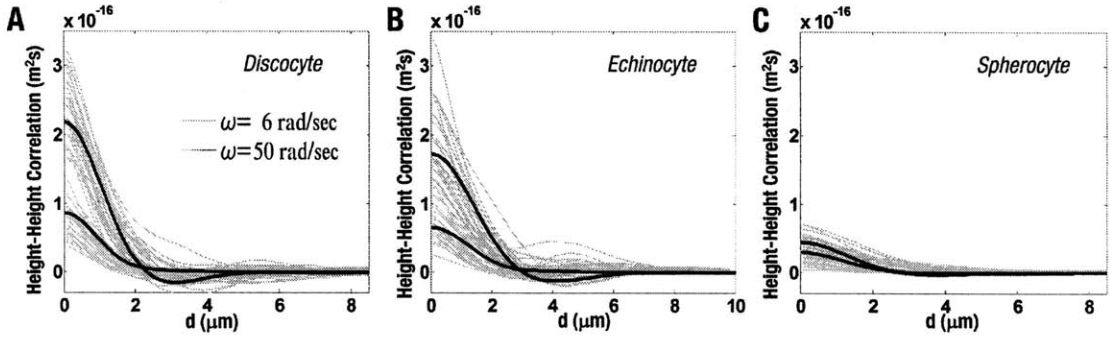

Figure 12 Height-height correlation function from experiments (faint lines, N=30 per each group) and calculation (thick lines). A-C, height-height correlation function as a projected distant for DCs (A), ECs (B), and SCs (C) for ω = 6 rad/sec (blue) and ω = 50 rad/sec (red).

The parameters extracted from the fit are shown in Figure 13A-C. The extracted bending modulus increases significantly during the DC-EC-SC transition ($p < 10^{-7}$. Their mean values are 6.3±1.0 (DC), 11.9±2.5 (EC), and 23.8±4.1 (SC) in units of k_BT, as shown in Figure 13C. These values are in general agreement with those expected for a phospholipid bilayer (5 – 20)×k_BT[71]. The increase in bending modulus suggests changes in the composition of the lipid membrane. In particular, experiments have shown that a 30% increase of cholesterol causes a three-fold increase in bending modulus of lipid membranes[72-73].We measured directly the change in surface area of RBCs during the transition from DC to SC morphologies and found a 31% decrease in surface area

(not accounting for surface area stored in fluctuations). This surface area decrease must be accompanied by loss of lipids, via microvesiculation. Previous work indicates that, after vesiculation, RBCs indeed have a higher cholesterol/phospholipid ratio and a lower phosphatidylserine/phospholipid ratio compared to the exovesicles shed from the parent RBCs[74]. Thus, there is evidence that there is a significant change in lipid composition of the RBC bilayer during the morphological changes from DC to EC and SC and these changes in lipid composition can generate the observed changes in the bending modulus.

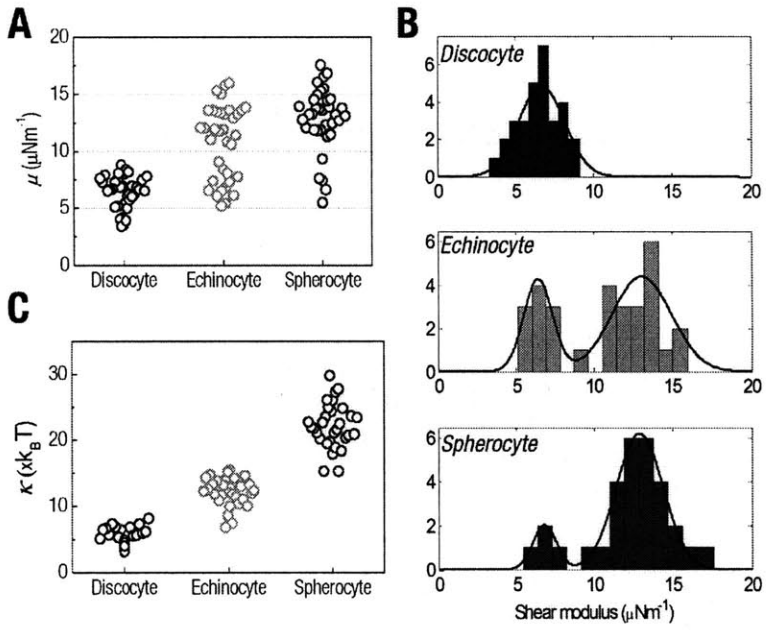

Figure 13 Shear modulus and bending modulus. A, Shear moduli of DCs, ECs, and SCs with their mean values represented by the horizontal lines. *p*-values verify that the differences in the shear moduli between morphological groups are statistically significant: $p < 10^{-5}$ between DCs and ECs, and between DCs and SC; $p < 10^{-4}$ between ECs and SCs. B, Distributions of shear moduli. The Gaussian fits are overlapped. The centers of the Gaussian fits are 6.7 (DCs), 6.4 and 13.0 (ECs), and 6.8 and 12.9 (SCs). C, bending modulus of three groups. The mean of bending moduli (shown by horizontal lines) are 5.3 ± 1.2, 11.8 ± 2.3, and 22.5 ± 3.3, respectively ($p < 10^{-7}$ between both DCs - ECs and ECs - SCs.)

The shear modulus results are shown in Figure 13A-B. The fitted shear moduli are 6.4±1.4 (DC), 10.7±3.5 (EC), and 12.2±3.0 (SC) in μNm^{-1}. These values are consistent with earlier work based on micropipette aspiration[16] and optical tweezers[31]. The magnitude of the measured shear modulus also agrees well with simple elastic models of the spectrin network. We calculated the shear modulus of a disorder-free triangular network of wormlike chain elastic elements[75]. Taking typical values for the lattice constant of the network (90 nm) and persistence length (7.5 nm)[76], we find that the network shear modulus of 5 μNm^{-1} requires a spectrin contour of 197 nm. This contour length is consistence with the previously published value of 194 nm [77].

The shear modulus of SCs and ECs increased by roughly a factor of two compared to the DCs ($p < 10^{-5}$). There is, however, significant cell-to-cell variation in the shear modulus. While the histogram of shear moduli of DCs can be fit by a single Gaussian distribution centered at 6.7 μNm^{-1}, the analogous shear moduli distributions for ECs and SCs are bimodal, with peaks at, respectively, 6.4 μNm^{-1} and 13.0 μNm^{-1} (ECs), and 6.8 μNm^{-1} and 12.9 μNm^{-1} (SCs) (Figure 13B). These data suggest that there are essentially two independent conformations of the spectrin network: a soft configuration ($\mu \approx 7\ \mu Nm^{-1}$) and a stiff one ($\mu \approx 13\ \mu Nm^{-1}$). Essentially all DCs have the soft configuration, but the morphological transition to EC and then SC promotes the transition to the stiff network configuration.

Given the well-known extension-hardening of a wormlike chain[78], one might hypothesize that the stiff state of the spectrin network results from simply stretching the individual filaments. The observed stiffening would require approximately a 50% extension of the lattice constant of the spectrin network during the DC-EC-SC transition. However, such a stretch is incompatible with the observed area *decrease* of the membrane during this morphological transition. From the topographical information measured by DPM, we calculate mean surface areas of 139.4 (DC), 143.4 (EC), and 96.3 (SC) in μm^2. Thus, we propose that the observed morphological changes must be accompanied by modifications of the spectrin elasticity, the connectivity of the network, or its attachment to the lipid bilayer.

3.2. OSMOTIC EFFECTS

The physical properties of living cells are exquisitely sensitive to their physical and chemical environment. Complex multi-cellular organisms typically maintain a sophisticated feedback system, known collectively as homeostasis, to control these variables and ensure the continued physiological function of the cell. For example, red blood cells (RBCs) do not have an autonomous regulatory system maintaining cell volume. Instead the blood serum is maintained at fixed osmolality to control the flux of water to the circulating RBCs. When placed in hypotonic solutions (i.e., solutions with a lower concentration of solutes), the hemoglobin (Hb)-rich interior of the RBCs has a lower chemical potential for water. Water enters the cells through the lipid membrane, causing swelling and, in extreme cases, bursting the cells. Alternatively, RBCs shrink when placed in hypertonic solutions, as the osmotic pressure difference forces water out of the cytosol of the RBCs.

In addition to changing the cells' morphology, these volume changes driven by osmotic pressure variations modify the mechanics of the cells. Since RBCs do not have an internal cytoskeleton or other complex sub-cellular organelles, their mechanics is determined entirely by their membrane, which is a lipid bilayer coupled to a triangular lattice of semiflexible polymer filaments mainly composed of spectrin. Any observed change in the mechanics of the cells under osmotic stress must reflect the elastic nonlinearity of this composite membrane as it is tensed or relaxed by the influx or respectively efflux of water. Thus, the ability to measure the *linear response* properties of the cell membrane at varying states of osmotic stress allows one to experimentally probe the *nonlinear elastic response* of this tethered membrane.

In this section we report on a series of microrheological measurements of RBC membrane mechanics obtained at varying levels of osmotic stress. We simultaneously measure the cellular volume so that we may quantitatively measure the change in the elastic properties of the composite membrane as a function of applied strain. Our results provide insight into the general problem of the nonlinear mechanics of tethered membranes but also have biological implications for understanding the effects of blood serum osmolality on RBC mechanics. Since these cells undergo large deformations and significant changes in osmotic stress in the microvasculature, understanding the nonlinear mechanics of RBCs under osmotic pressure may have direct physiological implications.

3.2.1. MORPHOLOGIES OF RBC UNDER DIFFERENT OSMOTIC PRESSURES

In this study we use cellular microrheology to probe the effective linear elastic response of the membrane at varying states of stress, controlled by an external osmotic pressure. To modulate the osmolality of the medium, we prepared RBC suspensions (10^6 cell/μl) with eleven different osmolalities ranging from 100 to 600 mOsm/kg H_2O. Fresh blood samples were collected and diluted 1:5 in Hank's buffer saline solution (HBSS) and then immediately centrifuged at 2000 g at 5°C for 10 minutes to separate RBCs from plasma. The RBCs were washed three times and then resuspended in the given NaCl solutions. The NaCl solutions contained increasing concentrations of NaCl (0.3-1.8)%, which correspond to suspension osmolalities ranging from 100-600 mOsm/kg. Using DPM we extracted quantitative optical phase shifts $\phi(x,y,t)$ associated with the cells, at spatial and temporal resolutions of nm and ms, respectively [37, 45]. The cell thickness profile is obtained from the optical phase shift as $h(x,y,t)=(\lambda/2\pi\Delta n)\phi(x,y,t)$. Since the refractive index difference, Δn, is mainly contributed from homogeneous Hb solution in cytoplasm, the integration of optical phase shifts over cell area, i.e. the dry mass [48], is related to the volume of RBC as, $Volume = \int \langle h(x,y) \rangle dA$. The Δn was calculated using the RBC volume data in the literature[79].

3.2.2. MEMBRANE DYNAMICS OF RBC MEMBRANES UNDER DIFFERENT OSMOTIC PRESSURES

Thickness profiles and horizontal cross-sections of RBCs in hypotonic, isotonic, and hypertonic media are shown in Figure 14. It is clear that different osmolalities of the extracellular medium result in significant changes in RBC shape. In a hypotonic medium (100 mOsm/kg, Figure 14a), RBCs are swollen due to water influx but still maintain the dimpled region in the center. At the osmotic pressure less than 100 mOsm/kg, most of RBCs are lysed. In the hypertonic case (600 mOsm/kg, Figure 14), RBCs shrink due to water efflux. In a hypertonic medium, the projected area of the membrane is lower than that of normal RBCs, which is indicative of an increase in the membrane tension caused by cell swelling; see Figure 15a.

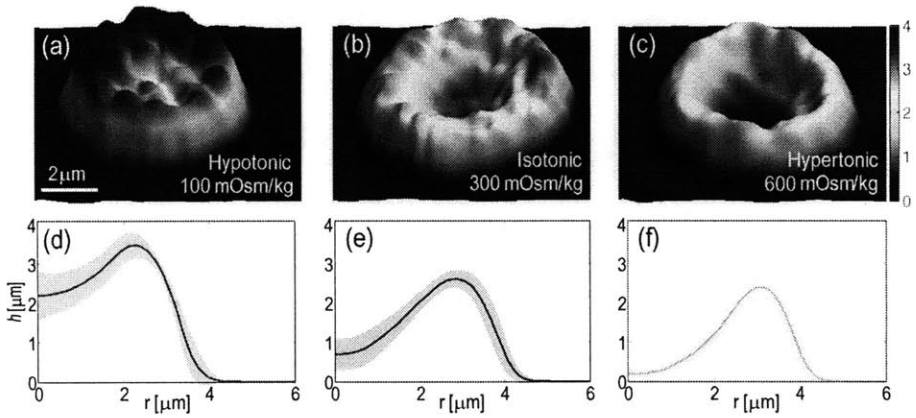

Figure 14 (a-c), Topography of a RBC exposed to hypotonic (a), isotonic (b), and hypertonic (c) solutions. (d-f), Corresponding membrane height as a function of a distance from the center of cells. Thick lines show the average values and the shaded areas represent standard deviations for 20 RBCs.

In contrast, the projected area in a hypertonic medium does not change significantly. We extracted the mean corpuscular hemoglobin (MCH), i.e., the total amount of Hb in the cell, as the product of the Hb concentration and cytoplasmic volume. The Hb concentration was retrieved using its known relationship with the refractive index [51]. MCH maintains constant values at different osmolalities (Fig. 2c), which is consistent with the impermeability of the RBC membrane to large Hb proteins.

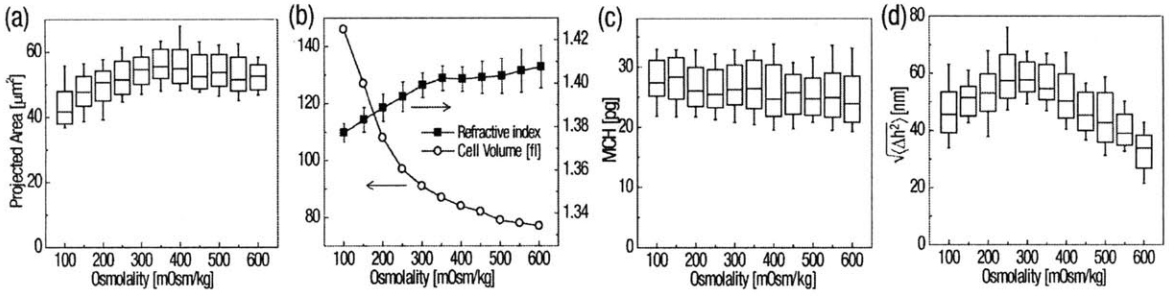

Figure 15 (a) Projected areas of RBCs at different osmolalities. (b) Averaged refractive index of RBC cytoplasm (closed symbols) and RBC volume calibrated from Ref. [79] (open symbols). (c) MCHs at different osmolalities. (d) RMS fluctuations in RBC membrane. Each box represents standard deviation for 20 RBCs, center line for median and whisker for min-max data.

The membrane fluctuations were obtained by subtracting the time-averaged cell profile from each instantaneous topography map in the series, $\Delta h(x,y,t) = h(x,y,t) - \langle h(x,y) \rangle$. The root mean squared (RMS) displacement of membrane fluctuations, $\sqrt{\langle \Delta h^2 \rangle}$, shows that the maximum membrane fluctuations occur around 300 mOsm/kg, which is within the normal physiological blood osmolality (Figure 15d). The decreased deformability of RBCs in both hypo- and hypertonic conditions is consistent with a variety of experimental techniques including laser scattering, cell elongation measurements, and blood filtration experiments [80-81].

3.2.3. RBC MECHANICS UNDER DIFFERENT OSMOTIC PRESSURES

In order to investigate the mechanical properties of RBCs, we analyze the spatial correlations of the out-of-plane membrane fluctuations using a continuum model of the composite spectrin-network/lipid membrane [58]. Our recent theoretical description incorporates the coupling between the bending and compression modes of the curved membrane [58] and allows us to determine quantitatively the cell's mechanical parameters: κ, K_A, μ, η_c. The details of the model have been discussed in the earlier section. The two-point correlation function of the membrane fluctuations was calculated as $C(d,t) = \langle \Delta h(d,t)\Delta h(0,0) \rangle$, where the angular brackets denote both spatial and temporal averaging. As shown in Figure 16, the theoretical model provides a very good description of the experimental data, which allows us to extract the cell material properties. In addition, we find that there is generically a single best fit, as many of the different features of the correlation function are controlled primarily by one parameter.

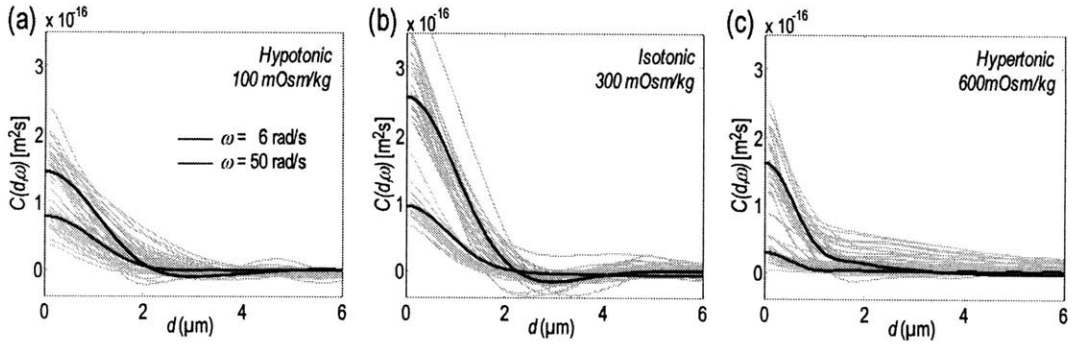

Figure 16 (a-c), Height-height correlation of RBC membrane fluctuations as a function of projected distance, in hypotonic (a), isotonic (b), and hypertonic (c) solutions. The faint lines are the experimental data for individual RBCs (N=20 per each group), while the thick lines are the theoretical curves using the averaged fitting parameters.

To obtain these fits to $\tilde{C}(d,\omega)$, we adjust the following parameters: the shear μ and area compression K_A moduli of the spectrin network and lipid bilayer, the bending modulus κ of the lipid bilayer, the viscosity of the cytosol η_c and the radius of the sphere R[54]. We constrain our fits by setting R to the average radius of curvature of the RBC obtained directly from the data and fixing the viscosity for extracellular medium to be η_s =1.2 mPa·s [68]. Furthermore we assume that the elastic properties of composite membrane are dominated by reactive and not dissipative terms, so that we may treat the elastic constants as real and frequency-independent. This assumption is supported *a posteriori* by making fits to correlation functions at two frequencies separated by a factor of ~ 8 with the same elastic parameters. This leaves a four dimensional space of fitting parameters spanned by κ, K_A, μ, and η_c. For a triangular elastic network we expect $\mu = \lambda$ [70] so positive values of dimensionless parameter $\delta = K_A/\mu - 2$ measures the importance of the contribution of the lipid bilayer's surface tension to the effective area compression modulus of the composite membrane.

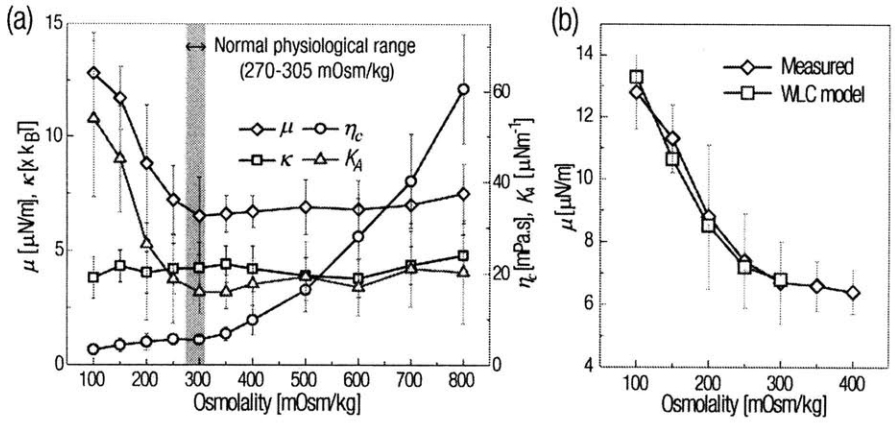

Figure 17 (a) Shear modulus μ, cytosol viscosity η_c , and bending modulus κ versus different osmotic pressure. Error bar represents standard deviation for 20 RBCs. (b) The observed increase in μ of the membrane (black line) compared to a simple WLC prediction for the nonlinear increase in μ associated with the tensing of the membrane (red line).

From these fits we determined the three mechanical properties of RBC membrane in different osmolalities (Figure 17). We also extracted the viscosity of the cytosol by fitting the fluctuation data at two frequencies; the viscosity generates the only frequency-dependent stress. The shear modulus of spectrin network μ in hypotonic medium shows a significant increase compared to the normal and hypertonic cases. Interestingly, μ does not change above 300 mOsm/kg. As expected the spectrin network becomes significantly less compliant ($\mu \approx 13$ μNm^{-1}) under tension. We model the spectrin network as a perfect triangular lattice of semiflexible worm-like chain (WLC) filaments, using a standard value for the thermal persistence length of spectrin $\ell_P = 7.5\ nm$. At physiological osmolality (300 mOsm/kg), we can account for the observed shear modulus using a standard value for the lattice constant of the spectrin network at physiological osmolality $a_0 = 90$ nm and assuming that the spectrin contour length between nodes of the network is 170 nm, which is close to previous measurements [68]. We now assume that lower osmolality leads to a uniform extension of the spectrin lattice constant: $a(V) = a_0(V/V_0)^{1/3}$, where V_0 is the volume of the cell at physiological osmolality and V is the measured volume under osmotic stress. From this extension of the lattice and the WLC model [82] we determine the effective spring constant of the stretched spectrin in the osmotically stressed cells, which allows predictions of the RBC shear modulus without additional fitting parameters. The results fit the observed increase in the shear modulus remarkably well. The area compression modulus K_A also increases as the membrane is tensed by the osmotic stress. This increase, however, is stronger than that predicted by the WLC model, showing the importance of the lipid bilayer's surface tension in determining this elastic constant. This is not surprising: $\delta \approx 0.4$ even for the low membrane tensions present at physiological osmolality, demonstrating the significant role of the bilayer in K_A.

The membrane bending modulus, on the other hand, does not show a significant dependence on osmolalities ($\kappa \approx 5 \times k_BT$). This indicates that the composition of the RBC bilayer

does not change with osmotic stress. Finally, the viscosity of the cytosol η_c increases monotonically with increasing osmolality since water leaves the cell (through aquaporin-1 channels) increasing the cytoplasmic Hb concentration, resulting in an increase of cytosolic viscosity [83]. We speculate that large changes in the cytosolic viscosity may have a physiologically protective effect. By increasing viscous dissipation when RBCs pass through the small capillaries of the kidney, where the osmolality can be as high as 1200 mOsm/kg, the viscous stresses in cytosol may reduce in-plane membrane stresses and prevent cell lysis as they undergo large-scale deformation.

We have used the dynamic fluctuations RBCs under varying osmotic stress to measure the nonlinear response of the composite membrane's shear modulus, bending modulus, and area compression modulus. By examining data at different frequencies we also obtain the cytosolic viscosity. We find that under tension the composite membrane is strongly strain hardening in both shear and area moduli. The shear modulus enhancement is easily understood in terms of the WLC model. Further work is needed to understand the nonlinear stiffening of K_A under tension. As expected, the bending modulus is highly insensitive to imposed osmotic stress and the cytosolic viscosity increases with Hb concentration. These elastic constants are all relatively insensitive to membrane relaxation in hypertonic solutions. Understanding this point may require more sophisticated models that include steric interactions between parts of the membrane. Finally, we note that the RBC moduli reach their minimal values at physiological osmolality, perhaps reflecting some evolutionary tuning of these elastic nonlinearities.

CHAPTER 4. RBC MECHANICS PART II: PATHOLOGICAL EFFECTS

4.1. INFECTION OF *P.FALCIPARUM*[6]

During the intra-erythrocytic development, the malaria parasite *Plasmodium falciparum* causes structural, biochemical and mechanical changes to host RBCs. Major structural changes include the parasitophorous vacuoles that surround the growing parasites in their host RBCs, loss of cell volume, and the appearance of small, nano-scale protrusions or "knobs", on the membrane surface [85]. From the biochemical standpoint, a considerable amount of hemoglobin (Hb) is digested by parasites during intra-erythrocytic development and converted into insoluble polymerized forms of heme, known as hemozoin [86-87]. Hemozoin appears as brown crystals in the vacuole of parasite in later maturation stages of *Pf*-RBCs.

Two major mechanical modifications are loss of RBC deformability [88-90] and increased cytoadherence of the invaded RBC membrane to vascular endothelium and other RBCs [91]. These changes lead to sequestration of RBCs in microvasculature in the later stages of parasite development, which is linked to vital organ dysfunction in severe malaria. In the earlier stage, where some loss of deformability occurs, *Pf*-RBCs continue to circulate in blood stream.

Membrane dynamics of RBCs can be influenced by human disease states. Fluctuations in phospholipid bilayer and attached spectrin network are known to be altered by cytoskeletal defects, stress, and actin–spectrin dissociations arising from metabolic activity linked to adenosine-5'-triphosphate (ATP) concentration [17, 30, 65, 92-93]. Proteins transported from invading organisms, such as the virulent malaria-inducing parasite *P. falciparum*, to specific binding sites in the spectrin network are considered to introduce significant alterations to RBC membrane dynamics and mechanical response [5, 18]. These changes could provide insights into possible mechanistic pathways in the pathogenesis of malaria, as the parasite alters biophysical properties of RBCs during its intra-erythrocyte stage that lasts up to 48 hours. Despite the broad realization that membrane fluctuations provide information on critical interactions among sub-cellular structure, mechanical stress, and biochemical links between the cell interior and the external environment, systematic experiments of cell membrane dynamics, over the physiologically relevant temperature range, have not been performed.

A clinical feature of symptomatic *P. falciparum* malaria is the presence of periodic episodes of high fever. Previous studies report that fever influences *P. falciparum* survival rate and deformability of *Pf*-RBCs [5]. Specifically, loss of deformability at ring stage was found to be more severe at febrile temperature (41°C) compared to physiological temperature (37°C). However, *in vitro* experiments at febrile and physiological temperature only reveal a partial story of what is experienced *in vivo*. When physiological temperature is restored after a fever episode, infected

---

[6] This chapter is modified from Ref.[84] with the publisher's permission.

RBCs in circulation might not fully recover properties typically observed at physiological temperature. If the changes to deformability observed at fever conditions are irreversible, prior effects of fever on *Pf*-RBCs would remain. As a consequence, *Pf*-RBCs in circulation at physiological temperature may actually display deformability closer to those measured at febrile temperature. To explore this possibility, we measure the deformability of *Pf*-RBCs at physiological temperature after a transient exposure to febrile temperature to simulate the *in vivo* behavior after a febrile episode. When combined with deformability measurements at static physiological and febrile temperatures, these results give new and useful insights into how *Pf*-RBCs behave *in vivo*.

In this section, we present for the first time two intrinsic indicators that quantitatively and non-invasively elucidate the consequences on cell biomechanics of *P.falciparum* malaria: three dimensional distributions of refractive index and the membrane fluctuations in *Pf*-RBCs. The refractive index maps of *Pf*-RBCs show the morphological alterations of host RBCs and the structures of vacuoles of parasites. In addition, the refractive index is translated into quantitative information about Hb content of individual *Pf*-RBCs. During the intra-erythrocytic stages of *P. falciparum*, we show the decrease of both the total amount and the concentration of Hb in the cytoplasm of *Pf*-RBCs. Thermally driven membrane fluctuations in *Pf*-RBCs are strongly correlated with the material properties of cell membranes, which is significantly modified by the specific proteins exported by parasites during developmental stages. Fluctuations in *Pf*-RBCs membrane are used to characterize the membrane stiffness by determining the in-plane shear modulus. We present experimental results of membrane fluctuations in *Pf*-RBCs over the full range of intra-erythrocyte stages at both physiological and febrile temperatures, representative of malaria fever episodes. Parasite interactions with host RBC strongly correlate with temperature-dependent and stage-specific alterations to membrane dynamics. We critically assess the hypothesis that after exposure to febrile temperature, *Pf*-RBCs at physiological temperature display deformability closer to those at febrile temperature.

4.1.1 THREE DIMENSIONAL REFRACTIVE INDEX MAPS OF *PF*-RBCS

To quantitatively investigate the refractive index distribution of *Pf*-RBCs, we employed tomographic phase microscopy (TPM) [39]. TPM uses laser interferometry combined with rotating the incident beam, analogous to computed tomography (CT) in X-ray. TPM quantitatively provides the three dimensional distribution of refractive index, $n(x, y, z)$. As shown in Figure 18, we measured the refractive index maps of *Pf*-RBCs during all intra-erythrocytic stages: healthy RBC (Figure 18A), ring (Figure 18.B), trophozoite (Figure 18C) and schizont stage (Figure 18D). Images in the horizontal rows show refractive index maps at three different cross sections: 0.6 μm above the focused plane (top), at the focused plane (middle), and 0.6 μm below the focused plane (bottom). Whereas healthy RBCs show homogeneous distribution of refractive index, *Pf*-RBCs are not optically homogeneous. Many factors contribute to refractive index change: the vacuole of parasite occupies a fraction of volume in cytoplasm of RBC; Heme is released from hemoglobin digestion and converted into hemozoin crystals in the food vacuole of the parasite; and various parasite proteins are exported from parasite into cytoplasm of *Pf*-RBCs [94]. Regions of low refractive index indicate the vacuole of *P. falciparum* (black arrows in Figure 18B-D) and regions of high refractive index suggest the position of hemozoin (gray arrows in Figure 18C-D).

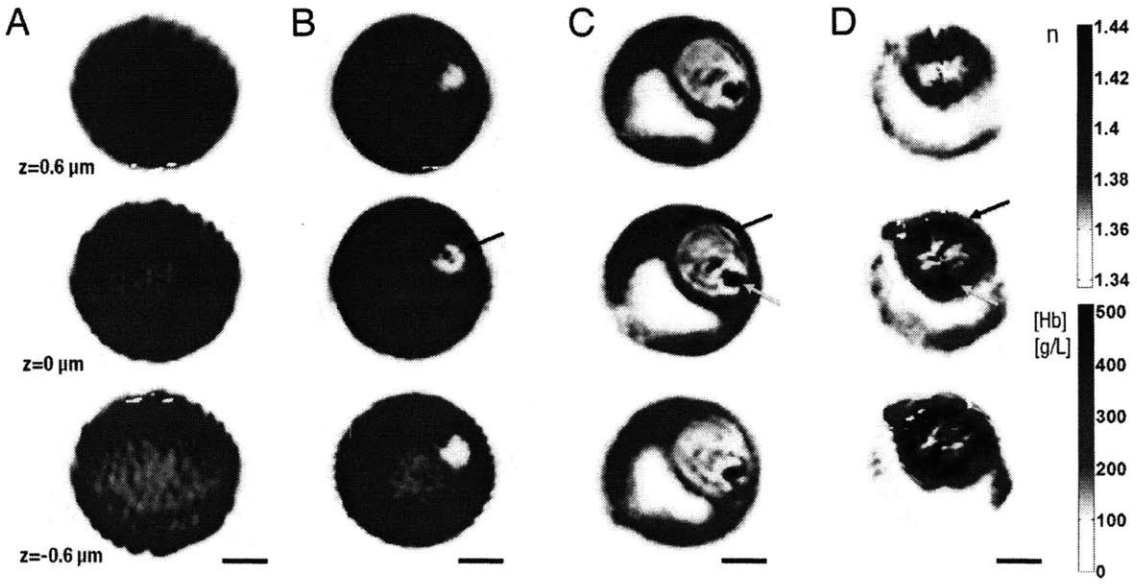

Figure 18 Three dimensional refractive index maps of *Pf*-RBCs reveal the structural modifications and the hemoglobin concentration of cytoplasm. (A) Healthy RBC, (B) Ring-stage, (C) Trophozoite-stage, (D) Schizont-stage. Images in row show three different cross sections: 0.6 μm above the focused plane (top), at the focused plane (middle), and 0.6 μm below the focused plane (bottom). Black arrows indicate the location of *P. falciparum*, and the gray arrows the location of hemozoin. Color-maps show the refractive index (*n*) (top right) and the Hb concentration (bottom right). Scalebar is 1.5 μm.

4.1.2. Hemoglobin content in individual *Pf*-RBCs

To quantitatively investigate the Hb content in *Pf*-RBCs we utilized refractive index maps measured by TPM. We averaged the refractive index over the cytoplasmic volume of *Pf*-RBC for 15 cells per group (Figure 19A). Their mean values are 1.399 ± 0.006, 1.395 ± 0.005, 1.383 ± 0.005, and 1.373 ± 0.006 for healthy RBCs, ring , trophozoite, and schizont stage, respectively. Given that the cytoplasm of RBCs consist mainly of Hb, it is likely that the refractive index is mostly due to the content of Hb. We calculated Hb concentration for individual *Pf*-RBCs by calibrating from the refractive index of Hb solutions reported in Ref. [51]. The results are shown in Figure 19B. The mean values of Hb concentration are 30.9 ± 3.1 g/dl, 29.3 ± 2.4 g/dl, 23.3 ± 2.7 g/dl, and 18.7 ± 2.9 g/dl for healthy RBCs, ring , trophozoite, and schizont stage, respectively. Since TPM also provides three-dimensional structural information, we calculate cytoplasmic volume of *Pf*-RBCs by subtracting the volume of parasites vacuole from the volume of whole RBC. The results are shown in Figure 19C. Their mean values are 93.1 ± 7.9 fl, 88.5 ± 11.8 fl, 57.5 ± 13.8 fl, and 34.2 ± 15.1 fl for healthy RBCs, ring, trophozoite, and schizont stage, respectively. In addition, we calculated total Hb contents per each *Pf*-RBC. The total amount of Hb in cytoplasmic volume is given by multiplying Hb

concentration and cytoplasmic volume. The results are shown in Figure 19D. Their mean values are 28.8 ± 1.2 pg, 25.9 ± 4.2 pg, 13.4 ± 3.4 pg, and 6.3 ± 2.5 pg for healthy RBCs, ring , trophozoite, and schizont stage, respectively.

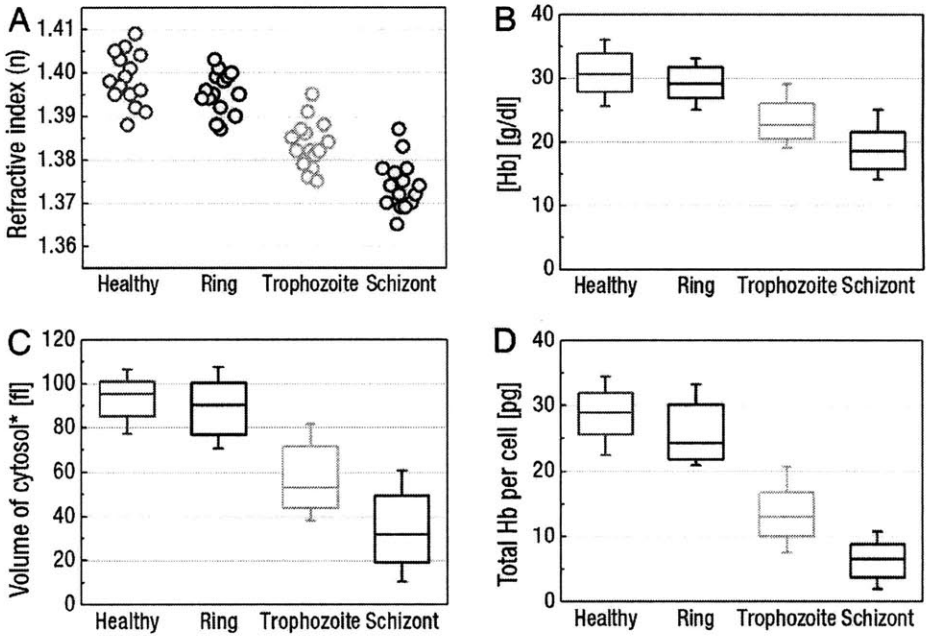

Figure 19 Host RBC hemoglobin concentrations decreases as *P. falciparum* matures. (A) Refractive index of healthy RBC and *Pf*-RBCs at the indicated stages, (B) Mean corpuscular Hb concentration (MCHC) of healthy and *Pf-RBCs* at the indicated stages, (C) Cytoplasm volume of *Pf-RBCs* at the indicated stages, (D) Hb content in healthy and *Pf-RBCs* at the indicated stages. Each point in A represents average refractive index for one cell. Graphs in B-D show the median (central horizontal line), standard deviations (box), and minimum and maximum values (vertical lines). For each condition 15 samples were tested.

4.1.3 Changes in morphology and deformability of Pf-RBCs during all intra-erythrocytic stages

To quantify the progressive alterations to RBC membrane fluctuations and mechanical response due to parasitization by *P. falciparum*, we employed diffraction phase microscopy (DPM). By extracting optical path-length shifts produced at each point across the cell, DPM quantitatively measures cell thickness information with spatial and temporal resolutions of nanometer and millisecond, respectively [36]. This information is then translated into the cell thickness profile, $h(x, y; t)$, by taking into account the optical homogeneity of the internal cell composition, which is captured through its refractive index.

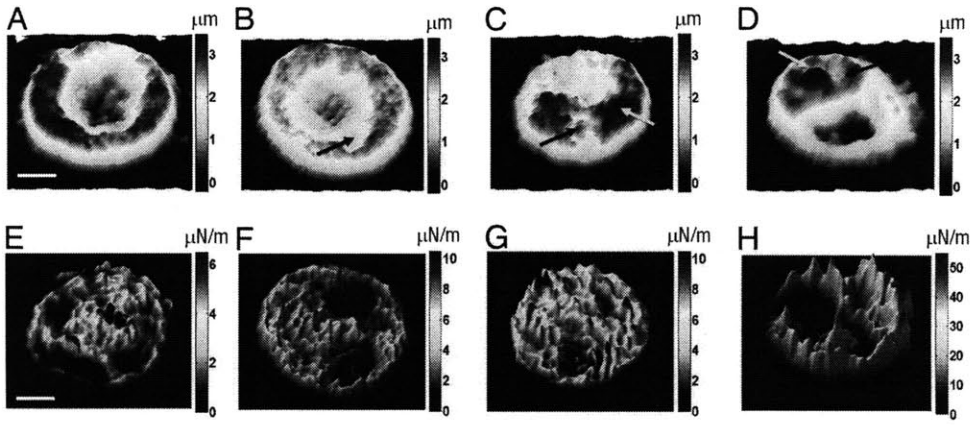

Figure 20 Topographic images and effective elastic constant maps of *Pf*-RBCs. (A & E) Healthy RBC, (B & F) Ring-stage, (C & G) Trophozoite-stage, (D & H) Schizont-stage. The topographic images in A-D are the instant thickness map of *Pf-RBCs*. The effective elastic constant maps are calculated from the root-mean-squared displacement of the thermal membrane fluctuations in the *Pf*-RBC membranes. Black arrows indicate the location of *P. falciparum*, and the gray arrows the location of hemozoin. (Bright-field and fluorescence micrographs provide information on locations of parasite and hemozoin; see SI text). Scalebar is 1.5 μm.

We used TPM to extract average values of refractive index of cytoplasm of healthy and *Pf*-RBCs. To investigate morphological changes of *Pf*-RBCs, we measured the instantaneous thickness profile, $h(x, y, t_0)$ of cells with DPM. Figure 20*A-D* show topographic images of healthy and *Pf*-RBCs at all stages of development. The effective stiffness map of the cell, $k_e(x, y)$ is obtained at each point on the cell, assuming an elastic restoring force associated with the membrane: $k_e(x, y) = k_B T / \langle \Delta h(x, y)^2 \rangle$, where k_B is the Boltzmann constant, T the absolute temperature, and $\langle \Delta h(x, y)^2 \rangle$ the mean-squared displacement. Representative k_e maps of RBCs at the indicated stages of parasite development are shown in Figure 20*E-H*. The map of instantaneous displacement of cell membrane fluctuation, $\Delta h(x, y, t)$, was obtained by subtracting time-averaged cell shape from each thickness map in the series. A histogram showing membrane displacements for all parasite stages is shown in Figure 21*A*.

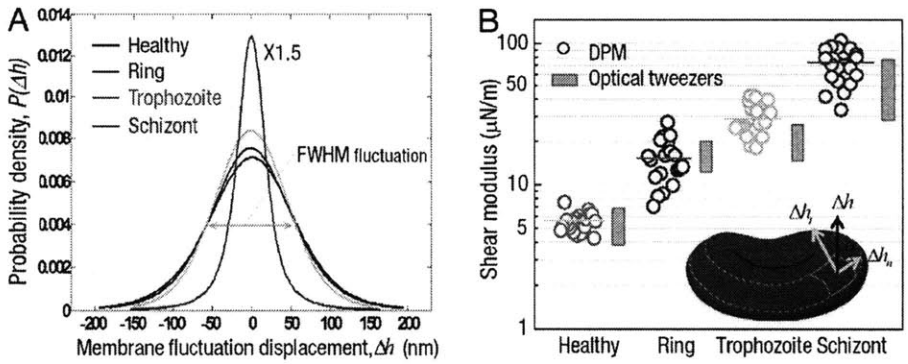

Figure 21 Membrane fluctuations and in-plane shear modulus at different intra-erythtocytic stages of *Pf*-RBCs. (A) Histograms of cell thickness fluctuation of *Pf*-RBCs (Histogram of the schizont stage is scaled down by a factor of 1.5), (B) In-plane shear modulus of the RBC membrane versus developmental stage of *Pf*-RBCs. The in-plane shear modulus is calculated from the in-plane membrane displacement, Δh_n over the rims of RBCs. Also shown for comparison are the estimated from optical tweezers [35]. *Inset*, Illustration of RBC and membrane fluctuations; Δh, thickness fluctuations measured by DPM. Δh_t, in-plane membrane displacement, Δh_n, out-of-plane membrane displacement, and α, the angle between Δh and Δh_t. The measurements are performed at the room temperature (23°C) and for each group 20 samples were tested.

RBC deformability is sensitive to membrane stiffness. Our DPM experiments provide quantitative information from which in-plane shear modulus of RBC membrane with attached spectrin cytoskeleton could be determined. The in-plane shear modulus *G* can be obtained using the Fourier-transformed Hamiltonian (strain energy) and equipartition theorem [95]:

$$G \approx \frac{k_B T \ln(A/a)}{3\pi \left\langle \Delta h_t^2 \right\rangle}, \tag{8}$$

where *A* is the projected diameter of RBC (~ 8 μm), and *a* is the minimum spatial wavelength measured by DPM (~ 0.5 μm). The tangential component of displacement in membrane fluctuations, Δh_t^2 is decoupled from axial membrane fluctuation Δh^2 using the angle α between the direction of Δh_t and the normal direction of membrane as illustrated in Figure 21*B inset*. The angle α is extracted from cell topographical information measured by DPM. The squared displacement component, Δh_t^2 was calculated and averaged along the circumference of the cell, from which in-plane shear modulus *G* was calculated. We determine that G = 5.5 ± 0.8 μN/m for healthy RBCs (Figure 21*B*), which compares well with independent modulus measurements, extracted for healthy RBCs from micropipette aspiration and optical tweezers [5, 16, 35]. The modulus for ring (G = 15.3 ± 5.4 μN/m), trophozoite (G = 28.9 ± 8.2 μN/m) and schizont (G = 71.0 ± 20.2 μN/m) stages is in good quantitative agreement with that inferred from large-deformation stretching with optical tweezers of *Pf*-RBCs over all stages of parasite maturation [35].

4.1.4. Effects of temperature on deformability of Pf-RBC during all intra-erythrocytic stages

The effect of febrile temperature exposure on deformability of *Pf*-RBCs is evaluated at each parasite stage. Measurements are made at physiological temperature (37°C), febrile temperature (41°C) and physiological temperature after 45 min exposure at 41°C (one fever cycle) using DPM. The results of these tests are summarized in Figure 22 (membrane fluctuation) and Figure 23 (in-plane shear modulus). The measured membrane in-plane shear modulus values reflect the overall cell deformability. The in-plane shear moduli for healthy RBCs are 6.2 ± 1.4, 4.9 ± 1.1, and 5.9 ± 1.0 in units of μN/m, respectively, for 37°C, 41°C, and 37°C after one fever cycle. For ring stage, 14.5 ± 3.8,

20.4 ± 7.2, and 13.5 ± 4.2 μN/m; for trophozoite stage, 35.0 ± 9.0, 56.6 ± 14.9, and 46.7 ± 13.4 μN/m; and for schizont stage, 71.8 ± 21.0, 95.0 ± 25.5, and 99.6 ± 21.6 μN/m, respectively. Previous work consistently reports a shear modulus of 4 – 8 μN/m for healthy RBCs at physiological and febrile temperature [5]. A higher shear modulus indicates a loss in deformability. As a control, healthy RBCs were evaluated at all three temperature conditions (Figure 22A and Figure 23A).

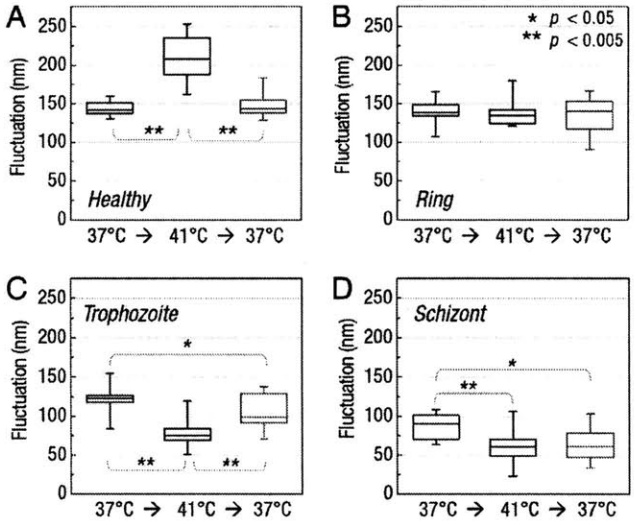

Figure 22 Membrane fluctuations of *Pf*-RBCs at different temperatures. Membrane fluctuation at different parasitic development stages at 37°C, 41°C, and 37°C after one fever cycle for (A) healthy RBCs, (B) ring-stage, (C) trophozoite-stage, and (D) schizont-stage of *Pf*-RBCs. The values for fluctuations are FWHM (full width half maximum) of the membrane fluctuation histograms. Graphs show the median (central horizontal line), standard deviations (box), and minimum and maximum values (vertical lines). The number of samples n=15 for each group.

Results from testing ring stage display a marked decrease in deformability at febrile temperature compared to physiological temperature (Figure 22B and Figure 23B). Upon returning to physiological temperature, the deformability of ring stage returned to the level observed before the fever episode. Similar to ring stage, measured shear modulus values for trophozoite and schizont stage increase at febrile temperature compared to physiological temperature. However, measurements at physiological temperature after one fever cycle indicate permanent changes to deformability as a result of fever conditions. In trophozoites, a partial recovery of deformability is observed after returning to physiological temperature (Figure 23C). Only half of the loss in deformability associated with a fever episode is recovered at the trophozoite stage. For schizonts stage, essentially all loss of deformability as a result of febrile temperature exposure is permanent and is not recovered after fever conditions end (Figure 23D).

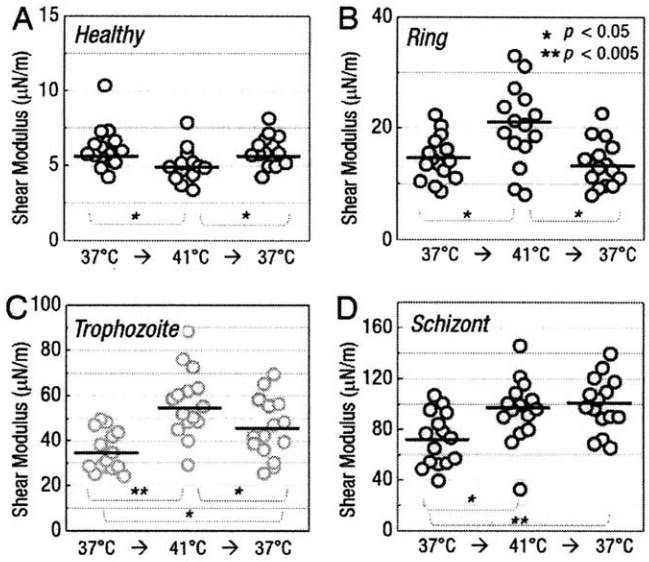

Figure 23 In-plane shear modulus of *Pf*-RBCs at different temperatures. In-plane shear modulus at different parasitic development stages at 37°C, 41°C, and 37°C after one fever cycle for (A) healthy RBCs, (B) ring-stage, (C) trophozoite-stage, and (D) schizont-stage. Symbols indicate individual *Pf*-RBCs. For each group 15 samples were tested.

4.1.5 Discussion

With *P. falciparum* parasitic development into the schizont stage, the normal discocyte shape is lost. Parasite modifications to the internal and membrane structure of invaded RBCs are implicated in the observed morphological changes (Figure 20*A-D*). Membrane stiffness also increases progressively with parasite development. In particular, the spatially averaged effective stiffness, $\langle k_e(x,y) \rangle$, at the schizont stage is up to an order of magnitude higher than that for healthy RBCs (Figure 20*E-H*). These results indicate that parasite development stage directly correlates with the amplitude of membrane fluctuations, and that the distribution of membrane fluctuations becomes much sharper with parasite development.

Interestingly, there is significant increase in membrane fluctuations (53% in the full width half maximum (FWHM) value of the fluctuation displacement histogram) from physiological to febrile temperature ($p < 0.01$), which is only a 7.5% increase in absolute temperature. Evidently, such enhancement in the fluctuation cannot be explained simply by equilibrium thermodynamics alone, i.e. the increase in the Boltzmann factor k_BT. This indicates that RBC phospholipid membrane and spectrin network undergo structural changes that alter elastic properties, which is reflected in changes to membrane in-plane shear modulus, G (Figure 21). One possible explanation is that a transitional structural change in spectrin molecular architecture occurs between physiological and febrile temperature, causing altered and reorganized cytoskeleton network. Both α- and β-spectrin molecules have a significant structural transition near 40 ºC [96]. It has been shown that membrane shear modulus of healthy RBCs decreases by about 20% when the temperature increases from 23 to 41 ºC [16]. From physiological to febrile temperature, membrane fluctuations decrease significantly

($p < 0.01$) for all infected test conditions (Figure 22), with trophozoite and schizont stages showing the strongest temperature-dependence. Based on comparison with results from healthy RBC and associated changes of in-plane shear modulus (Figure 23), we postulate that intra-erythrocytic parasite development causes an opposite effect. Parasite exported proteins that target RBC membrane can alter thermally induced spectrin folding transitions involved in stabilizing erythrocyte cytoskeleton [97]. Expression of *P. falciparum* genes is known to be affected by exposure to 41 ºC [98]. Under febrile conditions, increased levels of parasite-exported proteins could contribute to large changes in membrane fluctuations observed by DPM between physiological and febrile temperatures. One example is the ring-infected erythrocyte surface antigen (RESA). When RESA binds to spectrin, normal balance between spectrin dimers and tetramers in the cytoskeletal network is skewed towards tetramer formation, which results in increased membrane stability [6]. As a result, RESA enhances RBC resistance to mechanical and thermal damage. Moreover elevated thermal stability conferred by RESA plays a protective role for *Pf*-RBCs against damage at febrile temperature [7]. The possible specific role of other membrane proteins and histidine-rich proteins in influencing thermal and mechanical stability of RBCs over the temperature range of interest is presently not fully understood. The development of adhesion properties at the trophozoite and schizont stages can also contribute to significant decrease in fluctuation observed by DPM at these stages, especially at febrile temperature. For the same febrile temperature, our results indicate that fluctuation amplitude progressively decreases as a parasite develops from the ring to the schizont stage.

The findings presented in Figure 22-24 reveal that effects of fever episodes cause irreversible changes to deformability of *Pf*-RBCs. These experiments, for the first time, mimic *in vivo* conditions that *Pf*-RBCs experience to behavior at physiological or febrile temperature that cannot be examined by studying mechanical alone. Plastic behavior caused by a febrile episode is not observed at the ring stage. Decreased deformability observed under febrile conditions is recovered upon returning to physiological temperature. The decrease in deformability of *Pf*-RBCs may be attributed to exported parasite proteins that interact with the host RBC membrane. Their ability at the ring stage to regain deformability could play an important role in their ability to avoid splenic clearance when circulating. At the trophozoite and schizont stages, they displayed significant plastic changes to deformability. Again, the decreased deformability for mature stages may be also attributed largely to parasite exported proteins that associate with the membrane. Parasite protein exportation is likely accelerated by thermal energy. In turn, febrile episodes may be accelerating parasite protein exportation to the membrane that results in advancing the loss of deformability. Both reduced deformability and the development of adhesion properties contribute to sequestration at the trophozoite and schizont stages. The temperature-related permanent loss of deformability found in our experiments is greater than previously anticipated and can be viewed as an additional driving force to impede microcirculation and promote sequestration. The plastic behavior at the trophozoite and schizont stages in response to fever could also have implications when treatments are used to suppress fever episodes. Additional studies would be needed to explore this possibility.

Finally, the optical experimental techniques (TPM and DPM) used to measure the refractive index maps and the membrane fluctuations in this study offer unique advantages over other more commonly used techniques, such as micropipette aspiration, optical tweezers, laminar shear flow, and magnetic twisting cytometry. TPM quantitatively and non-invasively measures the three dimensional maps of refractive index, which provides a measure of Hb content of single *Pf*-RBCs. Indeed, TPM does not require any special sample preparation since the refractive index is an intrinsic optical property. DPM is able to measure nanometer level membrane fluctuations without any direct, and potentially invasive, contact with a cell. The optical layout of DPM is such that the sample temperature can be regulated easily without affecting of the rest of the apparatus, a common limitation of other techniques. In addition, deformability of living cells, measured by thermally driven membrane fluctuations, ensures mechanical properties in the linear regime. Also, measurements are made within seconds once a specific cell is identified. Thus, the technique provides the flexibility to experimentally sample a large number of samples under a variety of well-controlled test conditions in a reasonable time span.

4.3. Effects of ATP[7]

As they travel through small blood vessels and organs, RBCs undergo repeated severe deformation. The coupling and interactions between the phospholipid bilayer and the spectrin network govern the deformability of RBCs [100]. The fluid-like lipid bilayer is coupled to the two-dimensional spectrin network that comprises an approximately hexagonal lattice via protein junctional complexes. The RBC membrane is remarkably soft and elastic, and thus exhibits fluctuations with amplitudes of the order of tens of nanometers. The dynamics of the RBC membrane is strongly related to the membrane structure and mechanical properties, and has been explored extensively [55, 60, 66, 101-102]. However, experimental results available to date on RBC membrane fluctuations have provided only limited information on select regions of the cell membrane with limited spatial and/or temporal resolution (7-9). No full-field measurements of membrane fluctuations in the entire RBC arising in response to well-controlled metabolic activity have been made so far, and consequently, different techniques have led to different interpretations of the mechanistic origins of dynamic RBC membrane fluctuations with and without metabolic activity [103-105].

The RBC membrane is not a static but a metabolically regulated active structure. It is known that biochemical energy controls its static and dynamic characteristics. The presence of ATP is not only crucial in maintaining the biconcave shape of the RBC membrane [65], but has also been shown to increase the dynamic membrane fluctuations [103, 105]. However, the regulatory mechanism of ATP in RBC membranes still remains elusive. Furthermore, these static and dynamic effects of ATP on RBC membrane fluctuations have hitherto been regarded as separate phenomena and have never been explored simultaneously.

---

[7] This chapter is modified from Ref.[99] with the publisher's permission.

In this section, we present dynamic, full-field, and quantitative measurements of ATP effects on RBC membrane morphology and fluctuations. We show that in the presence of ATP, the RBC membrane fluctuations have a non-equilibrium, metabolic component in addition to a thermal one. The characteristics of this metabolically driven dynamics are observed only in the convex regions of the RBC membrane, with a periodic spacing on the order of the spectrin molecular network length scale. We demonstrate through systematic experiments that the metabolic energy of ATP dynamically remodels the coupling between a lipid layer and a spectrin network, which governs both the biconcave shape and non-equilibrium fluctuations in RBC membranes. Through these observations, we also rationalize the origins of differing mechanistic interpretations of RBC membrane fluctuations (commonly referred to as "flickering") specifically in the context of the role of ATP.

4.3.1. ATP EFFECT ON THE RBC MORPHOLOGY.

We first address the effects of ATP on the morphology of RBC membranes. RBC samples were prepared under four different conditions: healthy RBCs; RBCs with irreversibly depleted ATP; metabolically depleted ATP; and repleted ATP groups. After collection, a group of healthy RBCs was minimally prepared. For RBCs in the irreversibly depleted ATP group, the cytoplasmic pool of ATP was depleted by inosine and iodoacetamide. For the metabolically depleted ATP group, healthy RBCs were incubated in a glucose-free medium for 24 hours. For RBCs in the ATP repleted group, cytoplasmic ATP was first metabolically depleted, and then regenerated through the addition of D-glucose. To quantitatively measure the cell thickness map, we employed Diffraction Phase Microscopy [36-37]. By extracting the optical path-length shifts produced across the cell, we measured the cell thickness with nanometer sensitivity and millisecond temporal resolution. From the measured cell thickness profiles at a given time t, $h(x,y,t)$, we calculated time-averaged heights $\langle h(x,y)\rangle$ (Figure 24A-D). We observed the characteristic biconcave shape for healthy RBCs. When ATP was depleted, for both the irreversibly and the metabolically depleted groups, we observed loss of biconcave shape and echinocyte shape transformation. Reintroducing ATP resulted in the recovery of biconcave shape. This shows that ATP is crucial to maintaining the biconcave shape of RBCs [106].

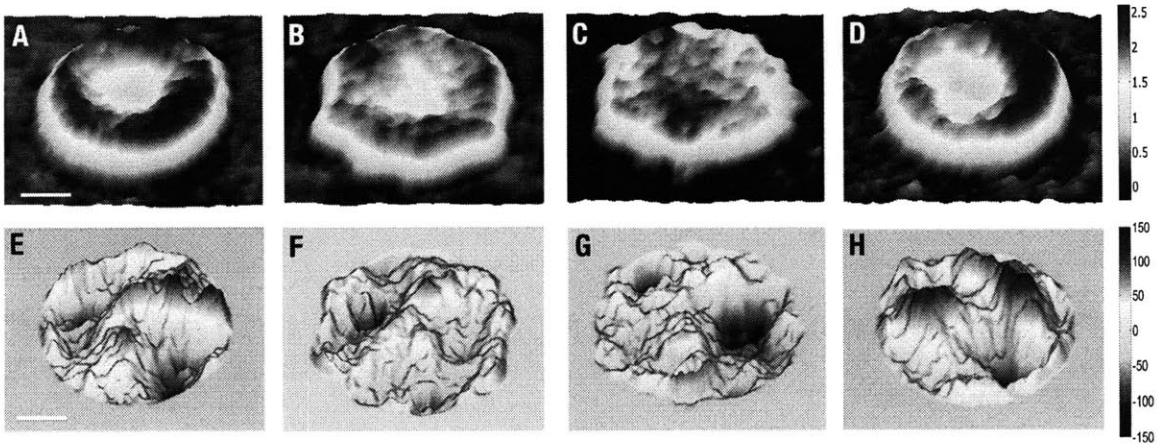

Figure 24 Effects of ATP on morphology and dynamic fluctuation in RBC membrane. Topography of a healthy RBC (A), of an ATP-depleted RBC (irreversible -ATP group) (B), of an ATP-depleted RBC (metabolic -ATP group) (C), and of a RBC with recovered ATP level (+ATP group) (D), respectively. (E-H), Instantaneous displacement maps of membrane fluctuation in the Figs. 1a-d, respectively. The scale bar is 2 μm. The colorbar scales are in μm and nm, respectively.

4.3.2. Enhanced membrane fluctuations in the presence of ATP.

To probe dynamic membrane fluctuations, we analyzed the membrane displacement map by subtracting the averaged shape from the cell thickness map, $\Delta h(x,y,t) = h(x,y,t) - \langle h(x,y) \rangle$ (Figure 24E-H). Compared to healthy RBCs, the fluctuation amplitudes were decreased in both ATP-depleted groups. Reintroducing ATP, however, increased the fluctuation amplitudes to healthy RBC levels. We calculated the root mean squared (RMS) displacement of membrane fluctuations, $\sqrt{\langle \Delta h^2 \rangle}$, which covers the entire cell area for 2 s at 120 frame/s (Figure 25). The RMS displacement of healthy RBCs is 41.5 ± 5.7 nm. Fluctuations significantly decreased to 32.0 ± 7.8 nm and 33.4 ± 8.7 nm in both the irreversibly metabolically ATP-depleted groups, respectively. However, the fluctuations in the ATP repleted group returned to the level of healthy RBCs (48.4 ± 10.2 nm). This is in agreement with an earlier report using the point measurement technique [65, 105].

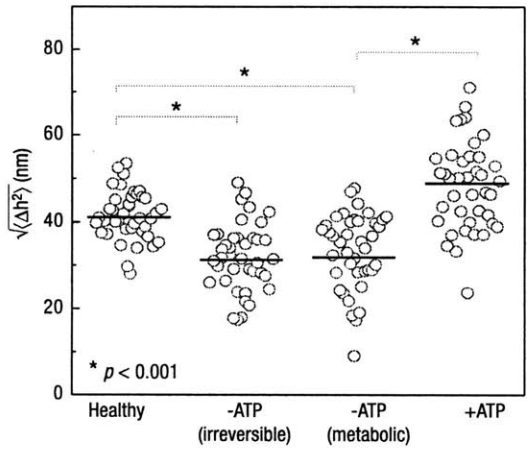

Figure 25 RMS displacements of membrane fluctuations for different ATP conditions: healthy RBCs, irreversibly ATP depleted RBCs, metabolically ATP depleted RBCs, and RBCs in which ATP was reintroduced to metabolically ATP-depleted RBCs. Each symbol represents an individual RBC and the horizontal line is the mean value.

4.3.3. ATP results in nonequilibrium dynamics for membrane fluctuations.

We showed that the membrane fluctuations indeed decrease in the absence of ATP, which is consistent with the previous results using point measurement techniques [103, 105]. However, this result does not yet answer the question of whether ATP drives 'active' non-equilibrium dynamics, or simply modifies membrane elastic properties. Of course, the two different situations can give rise to fundamentally different dynamics: (i) out-of-equilibrium fluctuations or (ii) equilibrium Gaussian fluctuations. In order to answer this question, we calculated the non-Gaussian parameter,

K, which is also known as kuritosis, for the membrane fluctuations (Figure 26A-D). Theoretically, K = 2 for purely thermally driven Gaussian motion and K increases above two for active non-equilibrium dynamics [93]. For healthy RBCs, the average value of K was 2.8, which shows that membrane fluctuations contain non-equilibrium dynamic components, particularly on short length and time scales (q > 5 rad/μm and Δt < 0.5 s). With depletion of ATP, K decreased to 2, as expected in purely thermally-driven dynamics (the average values of K were 2.06 and 2.19 for the irreversibly depleted and metabolically depleted ATP groups, respectively). Reintroducing ATP increased K to healthy RBC levels (average value K = 2.98). Our data clearly proves that active, metabolic energy from ATP contributes an enhancement in RMS displacements by 44.9%. This measured value is lower than predicted by a theoretical model, where an increase of at least 100% was expected [93]. However, it can be explained by recognizing that the ATP effect is more significant at large q-values, comparable with the size of the spectrin network [92]. For example, the ATP-mediated RMS displacement at q = 17 ± 0.5 rad/μm showed an increase of 143 % compared with the thermal components. Thus, in our overall assessment that includes all spatial frequencies, ATP enhancement is likely to be underestimated.

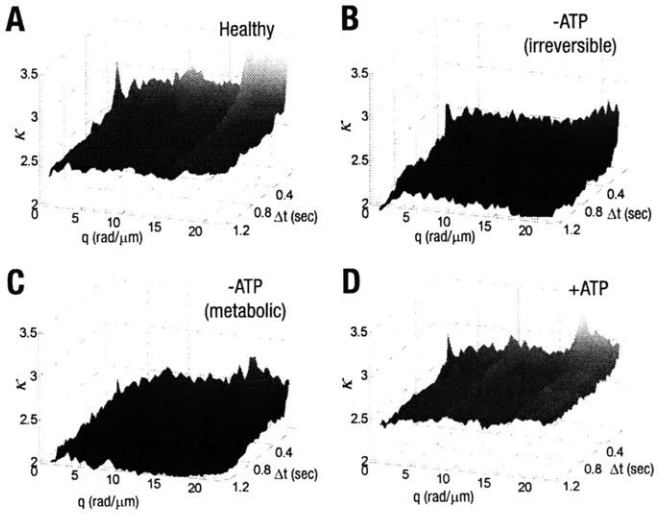

Figure 26 Non-equilibrium dynamic in RBC membranes. Averaged non-Gaussian parameter versus a lag time, Δt, and a spatial frequency, q, for membrane fluctuation in healthy RBC (A), irreversible ATP depletion group (B), metabolic ATP depletion group (C), and after reintroducing ATP to metabolic depletion group (D), respectively. The number of RBCs, N = 40 for each group.

Even though RBC membrane dynamics have been explored extensively, no definitive experiment has determined whether flickering is purely thermally driven or contains active contributions. First observed a century ago, its origin is generally believed to be thermal forces [66, 107]. Different interference-microscopic techniques have been employed to study membrane fluctuations and mechanical properties assuming Brownian dynamics [60, 101]. In contrast, a technique that qualitatively measured the local fluctuations of RBC membranes, reported a correlation between the ATP concentration and the fluctuation amplitude [65, 105]. However, recent experimental work, in which only edge shapes of RBCs were probed, showed no relation between ATP depletion

and membrane fluctuations [104]. Theoretically, RBC membrane fluctuations were traditionally studied using models of thermally driven equilibrium systems [66, 101]. A recent theoretical model [92, 108], validated by simulation [109-110], showed that local breaking and reforming of the spectrin network can result in enhanced fluctuations. Our results here showed that the depletion of ATP decreased the fluctuations in RBC membranes, which can be reversed when ATP is reintroduced. Furthermore, measurement of the non-Gaussian parameter κ revealed that the enhanced membrane fluctuations in the presence of ATP are indeed governed by nonequilibrium dynamics, and do not only reflect the change of the mechanical properties of RBCs.

4.3.4. BICONCAVE SHAPES ARE COUPLED WITH ATP-DEPENDENT ENHANCED MEMBRANE FLUCTUATIONS.

In order to study further spatial aspects of active motions, we analyzed the morphologies and fluctuations for RBCs in a polar coordinate system with its origin at cell center. Assuming cylindrical symmetry, the average height of the RBC membrane, $\langle h(r) \rangle$, and the membrane mean-squared displacements, $\langle h^2(r) \rangle$, are shown as functions of the radial distance, r (Figure 27). In healthy RBCs, the membrane fluctuations are enhanced and strongly localized at the outer convex region (the shaded are in Figure 27), while both ATP depletion groups showed little variation in membrane fluctuations over the cell surface. Remarkably, reintroducing ATP restores not only the biconcave shape, but also enhances the fluctuations in the outer convex area. This is striking because continuum equilibrium models predict a stronger restoring force and a decreased fluctuation amplitude in regions of high membrane curvature [111]. Our results show that active contributions are spatially inhomogeneous, and correlated with the maintenance of the biconcave shape. This strongly suggests that the RBC membrane cortex, especially the coupling and interaction between a lipid layer and spectrin network, is actively and dynamically remodeled in the presence of ATP. It also rationalizes different mechanistic inferences reported in the literature from prior measurement of membrane fluctuations [65, 103-104]. Probing the edge shape of RBCs alone does not capture ATP-dependent enhanced fluctuations [104] since they are localized on the convex region on RBC membrane and may not be significant only after 1 hour of ATP depletion. Point measurement techniques, which measure the averaged dynamics of the RBC membrane, could measure ATP-dependence [65, 103, 105].

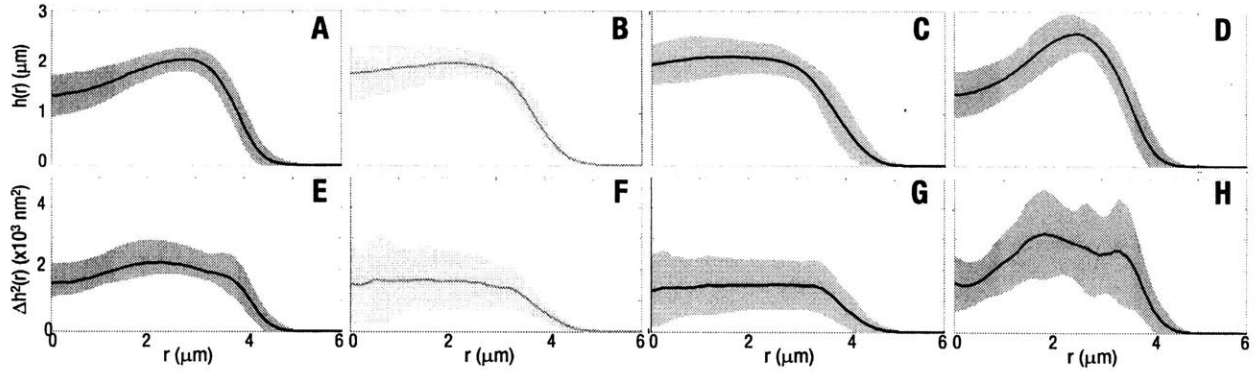

Figure 27 Correlation between biconcave shape and enhanced membrane fluctuations. (A-D), Averaged height as a function of the distance from the center of cells for healthy RBCs (A), for RBCs in the irreversibly ATP-depleted group (B), for RBCs in the metabolically ATP-depleted group (C), and for RBCs in which ATP was reintroduced to the metabolically ATP-depleted group (D), respectively. (E-H), Averaged squared height fluctuations as a function of the distance from the center of cells in Figs. 3a-d, respectively. Thick lines show the average value and the areas represent standard deviation for 40 RBCs.

4.3.5. SPATIAL ANALYSIS OF MEMBRANE FLUCTUATIONS.

Other cytoskeletons that contain actin, microtubules, and motor proteins such as myosin have demonstrated active motion [112] . However, this cannot be the case for the ATP-enhanced fluctuations in RBC because motor proteins are absent here. Then, how can the RBC exhibit active dynamics? To address this question, we further analyzed the results in the context of RBC cytoskeletal structure. The non-Gaussian parameter, K, at short time delays, was plotted as a function of spatial distance $\Lambda = 2\pi/q$ (Figure 28A). Interestingly, in the presence of ATP, K showed distinct peaks at specific distances (Λ = 361, 512, 680, 860, and 1030 nm). These peaks are equally spaced at 167 ± 10 nm, which indicates that ATP-dependent enhanced fluctuations are correlated with the network structure of the underlying cytoskeleton. Considering the roughly hexagonal lattice of spectrin network, these peaks can be related to the dynamic remodeling of the spectrin network by ATP. Possible elements responsible for this remodeling are the junctional complexes of the spectrin network that join six spectrin polymers by a short actin segment and protein-4.1 (Figure 28B). It was proposed that the ATP-induced remodeling takes the form of local associations and dissociations of spectrin filaments within the network or between the cytoskeleton and the lipid membrane [55, 92]. Both processes result in the formation of a structural defect in the hexagonal network, of size ~ 2Δ, where Δ is a distance between neighboring junctions (Figure 28C). This remodeling of the cytoskeletal attachment causes a local release of the cytoskeleton-induced membrane tension, and results in local bilayer deformation [55, 92]. The length-scale of this local, ATP-induced, bilayer deformation is therefore a multiple of the junction spacing, 2Δ. From the data we find Δ ~83.5 ± 5 nm, which is in good agreement with the separation of the junctions complexes measured by electron microscopy [113]. In addition, K at the short distance 2Δ was plotted as a function of a lag time (Figure 28D), which shows longer temporal correlations in the presence of ATP.

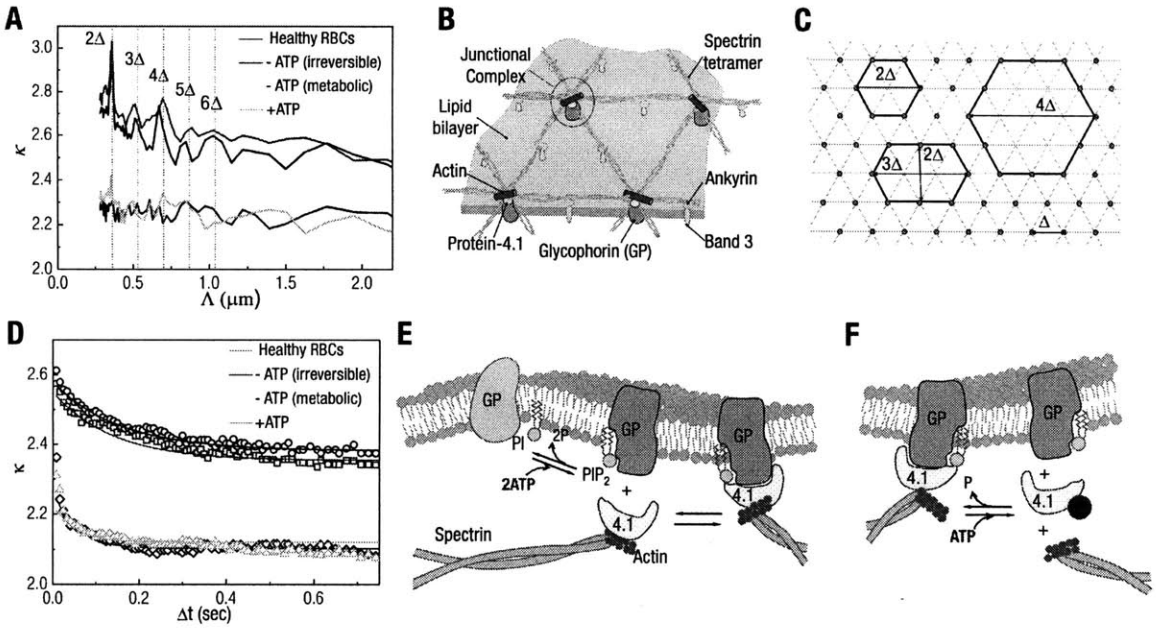

Figure 28 Cytoskeletal structure and enhanced fluctuations. (A), Non-Gaussian parameter at short time delay (Δt < 0.1 sec) as a function of spatial wavelength. The presence of ATP lead to non-thermal fluctuations, especially at Λ=361, 512, 680, 860, and 1030 nm. (B), Non-Gaussian parameter at short time delay as a function of lag time (Λ<350 nm). (C), Illustration showing the major proteins in the anchor complexes and the spectrin network. (D), Non-Gaussian parameter at spatial wavelength (q=15 rad/μm) as a function of a lag time. (E-F), models explaining the non-equilibrium dynamics in RBC membranes by phosphorylation of PI (E) and by phosphorylation of protein-4.1 (F).

4.3.6. ORIGIN OF THE ENHANCED FLUCTUATIONS.

The question then arises, how can ATP cause this dynamic remodeling of the cytoskeletal attachment? This may be related to protein phosphorylation powered by ATP, which is one of the physiological processes that control membrane stability. One possible candidate is the phosphorylation of the phosphoinositides (PI) because it consumes more ATP than the combined phosphorylation of all the membrane proteins [114]. PIP_2, phosphorylated from PI by ATP, is thought to play an important role in modulating the binding of the lipid bilayer to the cytoskeleton by altering the protein interactions that comprise the junctional complex at spectrin tetramer ends [115]. For example, PIP_2 strengthens the binding affinity of protein-4.1 to glycophorin C (GP) [116] (Figure 28E). Furthermore, PIP_2 dephosphorylation results in a decreased affinity for GP binding, and a subsequent detachment from spectrin network; the latter can result in increased membrane fluctuations since tension applied to the bilayer by spectrin network is locally and transiently released. In the absence of ATP, this dynamic remodeling may not occur, and thus RBCs exhibit only thermally driven membrane fluctuations. Another possibility is the phosphorylation of protein-4.1, which results in a reduced binding affinity between the actin, protein-4.1, and GP at the junction [117] (Figure 28F).

4.3.7. DISCUSSION

The phosphorylation-dependent binding of the cytoskeleton to the membrane can explain the correlation between nonequilibrium dynamic fluctuations and biconcave shape. Several models have been proposed to explain the biconcave shape of RBC [118], but it still remains as an unsolved puzzle. It was proposed that the ATP-regulated interaction between the junction complexes and the membrane plays a role in maintaining the biconcave shape [116]. A theoretical model, which relates ATP-induced unbinding to RBC shape, showed that this active process lowers the overall cytoskeleton shear rigidity and the tension that the spectrin network imposes on the membrane [92, 108]. Our results provide further experimental evidence for the metabolism-dependent shape transformation; we show that ATP-dependent transient binding of junctional complexes are localized over the cell outer area, and that the spectrin network should therefore exert a lower tension on the membrane. We also note that in the absence of ATP, the shapes of RBCs are similar to those of patients with hereditary elliptocytosis, where GP does not properly interact with protein 4.1, resulting in the lack of biconcave shape and deformability [15, 119]. This dynamic remodeling of the spectrin network offers a possible explanation for the observed metabolic dependence of red cell deformability [120]. Taken together, we have shown that the biconcave shape and nonequilibrium dynamics in the membrane are both consequences of the same biochemical activity: the dissociations of the cytoskeleton at the spectrin junctions, powered by ATP metabolism.

In summary, we have presented definitive evidence that membrane fluctuations in the RBC membrane have a metabolic as well as thermal energy component, which are localized at the outer area of the cell. Our results suggest that the spectrin-bilayer binding, through local remodeling of the spectrin junctions, give rise to these nonequilibrium dynamics. This remodeling is also important in determining cell deformability and the unique biconcave shape of RBCs. Our results are in good qualitative agreement with previously proposed theoretical models [92, 108]. The values measured for the ATP-mediated fluctuation amplitudes, which are lower than those predicted theoretically, can be understood by the spatial inhomogeneity of active motions. Whether this dynamic remodeling of the RBC cytoskeleton is beneficial in physiological conditions remains an open question, and it is now accessible to direct experimental study.

5. SUMMARY AND OUTLOOK

This thesis has presented a novel methodology to establish a non-contact optical imaging technique to retrieve the material properties of single red blood cells (RBCs) from their membrane fluctuations. We have developed an optical imaging technique to non-invasively quantify membrane fluctuations in red blood cells at the nanometer and millisecond scales[121]. This technique employs laser interferometry and provides full-field quantitative topographical information of living cells with unprecedented stability. Integration with a mathematical model has established a new methodology that provides specific material properties from individual cell membrane fluctuations: bending modulus; shear modulus of the membrane; and the viscosity of cytoplasm.

These properties have been used to systemically study the pathophysiology of human diseases affecting red blood cells. We have studied the mechanical properties of RBCs under various conditions including: (1) the morphological transition from discocyte to echinocyte, and to spherocyte; (2) different osmotic pressures; (3) parasitization by *P.falciparum* parasite; and (4) different amounts of metabolic energy.

We envision that this investigation could offer a means to link cell membrane fluctuations with the pathological conditions that lead to human disease states by quantifying the material properties of red blood cells, which may address a broader range of red-blood-cell biology problems concerning human health, disease diagnostics, therapeutics, and drug efficacy assays.

REFERENCES

1. Galinski, M.R., Medina, C.C., Ingravallo, P. & Barnwell, J.W. A reticulocyte-binding protein complex of Plasmodium vivax merozoites. *Cell* **69**, 1213?1226 (1992).
2. Salmon, B.L., Oksman, A. & Goldberg, D.E. Malaria parasite exit from the host erythrocyte: A two-step process requiring extraerythrocytic proteolysis. *Proc. Natl. Acad. Sci. U. S. A.*, 11413198 (2000).
3. Rug, M., Prescott, S.W., Fernandez, K.M., Cooke, B.M. & Cowman, A.F. The role of KAHRP domains in knob formation and cytoadherence of P falciparum-infected human erythrocytes. *Blood* **108**, 370 (2006).
4. Kemp, D.J., Coppel, R.L. & Anders, R.F. Repetitive Proteins and Genes of Malaria. *Annual. Rev. Microbio.* **41**, 181-181 (1987).
5. Mills, J.P. *et al.* Effect of plasmodial RESA protein on deformability of human red blood cells harboring Plasmodium falciparum. *Proc. Natl. Acad. Sci. U.S.A.* **104**, 9213-9217 (2007).
6. Pei, X. *et al.* The ring-infected erythrocyte surface antigen (RESA) of plasmodium falciparum stabilizes spectrin tetramers and suppresses further invasion. *Blood* **110**, 1036-1042 (2007).
7. Silva, M.D. *et al.* A role for the Plasmodium falciparum RESA protein in resistance against heat shock demonstrated using gene disruption. *Mol. Microbiol.* **56**, 990-1003 (2005).
8. Waller, K.L., Cooke, B.M., Nunomura, W., Mohandas, N. & Coppel, R.L. Mapping the Binding Domains Involved in the Interaction between the Plasmodium falciparum Knob-associated Histidine-rich Protein (KAHRP) and the Cytoadherence Ligand P. falciparum Erythrocyte Membrane Protein 1 (PfEMP1). *J. Bio. Chem.* **274**, 23808-23813 (1999).
9. Baruch, D.I. *et al.* Cloning the P. falciparum gene encoding PfEMP1, a malarial variant antigen and adherence receptor on the surface of parasitized human erythrocytes. *Cell* **82**, 77-87 (1995).
10. Trager, W. Erythrocyte knobs and malaria. *Nature* **340**, 352 (1989).
11. Crabb, B.S. *et al.* Targeted gene disruption shows that knobs enable malaria-infected red cells to cytoadhere under physiological shear stress. *Cell* **89**, 287-296 (1997).
12. Steck, T. The organization of proteins in the human red blood cell membrane: a review. *Journal of Cell Biology* **62**, 1 (1974).
13. NCI-Frederick (http://web.ncifcrf.gov/rtp/ial/eml/rbc.asp)
14. Hou, V. *et al.* Decrease in hnRNP A/B expression during erythropoiesis mediates a pre-mRNA splicing switch. *The EMBO journal* **21**, 6195-6204 (2002).
15. Suresh, S. Mechanical response of human red blood cells in health and disease: some structure-property-function relationships. *J. Mater. Res* **21**, 1872 (2006).
16. Waugh, R. & Evans, E.A. Thermoelasticity of red blood cell membrane. *Biophys. J.* **26**, 115-131 (1979).
17. Abbasakoor, F. & Boulos, P. Anal intraepithelial neoplasia. *British Journal of Surgery* **92**, 277-290 (2005).
18. Glenister, F.K., Coppel, R.L., Cowman, A.F., Mohandas, N. & Cooke, B.M. Contribution of parasite proteins to altered mechanical properties of malaria-infected red blood cells. *Blood* **99**, 1060-1063 (2002).
19. McGough, A.M. & Josephs, R. On the structure of erythrocyte spectrin in partially expanded membrane skeletons. *Proc. Natl. Acad. Sci. U. S. A.* **87**, 5208 (1990).

20. Lodish, H. *Molecular cell biology*. (WH Freeman New York:, 2000).
21. Chien, S. Red Cell Deformability and its Relevance to Blood Flow. *Annual. Rev. Physiol.* **49**, 177-192 (1987).
22. Ruestow, E. A look back: The Microscope. *Am J Gastroenterol* **10**, 3046 (1999).
23. Zernike, F. How I discovered phase contrast. *SPIE MILESTONE SERIES MS* **163**, 565-569 (2000).
24. Goldstein, J. *et al. Scanning electron microscopy and X-ray microanalysis.* (Plenum Pub Corp, 2003).
25. Binnig, G., Quate, C. & Gerber, C. Atomic force microscope. *Physical Review Letters* **56**, 930-933 (1986).
26. Bao, G. & Suresh, S. Cell and molecular mechanics of biological materials. *Nature Mat.* **2**, 715-725 (2003).
27. Radmacher, M., Fritz, M., Kacher, C.M., Cleveland, J.P. & Hansma, P.K. Measuring the viscoelastic properties of human platelets with the atomic force microscope. *Biophys. J.* **70**, 556-567 (1996).
28. Mijailovich, S.M., Kojic, M., Zivkovic, M., Fabry, B. & Fredberg, J.J. A finite element model of cell deformation during magnetic bead twisting. *J. Appl. Physiol.* **93**, 1429-1436 (2002).
29. Maksym, G.N. *et al.* Mechanical properties of cultured human airway smooth muscle cells from 0.05 to 0.4 Hz. *J. of Appl. Physiology* **89**, 1619-1632 (2000).
30. Discher, D.E., Mohandas, N. & Evans, E.A. Molecular maps of red cell deformation: hidden elasticity and in situ connectivity. *Science* **266**, 1032 (1994).
31. Dao, M., Lim, C.T. & Suresh, S. Mechanics of the human red blood cell deformed by optical tweezers. *J. Mech. Phys. Solids* **51**, 2259-2280 (2003).
32. Mohan, S., Mohan, N., Valente, A.J. & Sprague, E.A. Regulation of low shear flow-induced HAEC VCAM-1 expression and monocyte adhesion. *Am. J. Physiol., Cell Physiol.* **276**, 1100-1107 (1999).
33. Abate, E. *et al.* Combined performance tests before installation of the ATLAS Semiconductor and Transition Radiation Tracking Detectors. *Journal of Instrumentation* **3**, - (2008).
34. Puig-de-Morales-Marinkovic, M., Turner, K.T., Butler, J.P., Fredberg, J.J. & Suresh, S. Viscoelasticity of the human red blood cell. *Am J Physiol Cell Physiol* **293**, C597-605 (2007).
35. Li, J., Dao, M., Lim, C.T. & Suresh, S. Spectrin-Level Modeling of the Cytoskeleton and Optical Tweezers Stretching of the Erythrocyte. *Biophys. J.* **88**, 3707-3719 (2005).
36. Park, Y.K., Popescu, G., Badizadegan, K., Dasari, R.R. & Feld, M.S. Diffraction phase and fluorescence microscopy. *Opt. Express* **14**, 8263-8268 (2006).
37. Popescu, G., Ikeda, T., Dasari, R.R. & Feld, M.S. Diffraction phase microscopy for quantifying cell structure and dynamics. *Opt. Lett.* **31**, 775-777 (2006).
38. Amin, M. *et al.* Microrheology of red blood cell membranes using dynamic scattering microscopy. *Opt Express* **15**, 17001-17009 (2007).
39. Choi, W. *et al.* Tomographic phase microscopy. *Nat Methods* **4**, 717-719 (2007).
40. Park, Y.-K., Yamauchi, T., Choi, W., Dasari, R. & Feld, M. Spectroscopic phase microscopy for quantifying hemoglobin concentrations in intact red blood cells. *Opt. Lett* **34**, 3668-3670 (2009).
41. Barer, R. Determination of dry mass, thickness, solid and water concentration in living cells. *Nature* **172**, 1097-1098 (1953).
42. Cuche, E., Bevilacqua, F. & Depeursinge, C. Digital holography for quantitative phase-contrast imaging. *Opt. Lett.* **24**, 291-293 (1999).

43. Barty, A., Nugent, K., Paganin, D. & Roberts, A. Quantitative optical phase microscopy. *Optics Letters* **23**, 817-819 (1998).
44. Rylander, C. *et al.* Quantitative phase-contrast imaging of cells with phase-sensitive optical coherence microscopy. *Optics Letters* **29**, 1509-1511 (2004).
45. Park, Y.-K. *et al.* Refractive index maps and membrane dynamics of human red blood cells parasitized by Plasmodium falciparum. *Proc. Natl. Acad. Sci. U.S.A.* **105**, 13730 (2008).
46. Rappaz, B., Charriere, F., Depeursinge, C., Magistretti, P.J. & Marquet, P. Simultaneous cell morphometry and refractive index measurement with dual-wavelength digital holographic microscopy and dye-enhanced dispersion of perfusion medium. *Optics Letters* **33**, 744-746 (2008).
47. Park, Y.-K. *et al.* Speckle-field digital holographic microscopy. *Optics Express* **17**, 12285-12292 (2009).
48. Popescu, G. *et al.* Optical imaging of cell mass and growth dynamics. *Am. J. Physiol.: Cell Physiol.* **295**, C538 (2008).
49. Yang, C.H. *et al.* Interferometric phase-dispersion microscopy. *Opt Lett* **25**, 1526-1528 (2000).
50. Schiebener, P., Straub, J., Sengers, J. & Gallagher, J. Refractive index of water and steam as function of wavelength, temperature and density. *J. Phys. Chem. Ref. Data* **19**, 677-717 (1990).
51. Friebel, M. & Meinke, M. Model function to calculate the refractive index of native hemoglobin in the wavelength range of 250-1100 nm dependent on concentration. *Applied optics* **45**, 2838-2842 (2006).
52. Andersen, M., Painter, L. & Nir, S. Dispersion equation and polarizability of bovine serum albumin from measurements of refractive indices. *Biopolymers* **13** (1974).
53. Lichtman, M. *Williams hematology.* (McGraw-Hill Professional, 2005).
54. Park, Y. *et al.* Measurement of red blood cell mechanics during morphological changes. *Proceedings of the National Academy of Sciences* **107**, 6731 (2010).
55. Gov, N., Zilman, A.G. & Safran, S. Cytoskeleton Confinement and Tension of Red Blood Cell Membranes. *Phys. Rev. Lett.* **90**, 228101 (2003).
56. Cicuta, P., Keller, S.L. & Veatch, S.L. Diffusion of liquid domains in lipid bilayer membranes. *J Phys Chem B* **111**, 3328-3331 (2007).
57. den Otter, W.K. & Shkulipa, S.A. Intermonolayer friction and surface shear viscosity of lipid bilayer membranes. *Biophys J* **93**, 423-433 (2007).
58. Kuriabova, T. & Levine, A. Nanorheology of viscoelastic shells: Applications to viral capsids. *Phys. Rev. E* **77**, 31921 (2008).
59. Chaikin, P.M. & Lubensky, T.C. *Principles of Condensed Matter Physics.* (Cambridge University Press, 1995).
60. Popescu, G. *et al.* Optical Measurement of Cell Membrane Tension. *Phys. Rev. Lett.* **97**, 218101 (2006).
61. Fournier, J.B., Lacoste, D. & Rapha, E. Fluctuation Spectrum of Fluid Membranes Coupled to an Elastic Meshwork: Jump of the Effective Surface Tension at the Mesh Size. *Phys. Rev. Lett.* **92**, 18102 (2004).
62. Engelhardt, H., Gaub, H. & Sackmann, E. Viscoelastic properties of erythrocyte membranes in high-frequency electric fields. *Nature* **307**, 378-380 (1984).
63. Browicz, E. *Zentralbl. Med. Wiss.* **28** (1890).
64. Zilker, A., Ziegler, M. & Sackmann, E. Spectral-Analysis Of Erythrocyte Flickering In The 0.3-4-Mu-M-1 Regime By Microinterferometry Combined With Fast Image-Processing. *Phys. Rev. A* **46**, 7998-8002 (1992).

65. Tuvia, S., Levin, S., Bitler, A. & Korenstein, R. Mechanical fluctuations of the membrane-skeleton are dependent on F-actin ATPase in human erythrocytes. *J. Cell Biol.* **141**, 1551-1561 (1998).
66. Brochard, F. & Lennon, J.F. Frequency spectrum of the flicker phenomenon in erythrocytes. *J. Physique* **36**, 1035-1047 (1975).
67. Kaizuka, Y. & Groves, J.T. Hydrodynamic Damping of Membrane Thermal Fluctuations near Surfaces Imaged by Fluorescence Interference Microscopy. *Phys. Rev. Lett.* **96**, 118101 (2006).
68. Hochmuth, R.M., Buxbaum, K.L. & Evans, E.A. Temperature dependence of the viscoelastic recovery of red cell membrane. *Biophys. J.* **29**, 177-182 (1980).
69. Kelemen, C., Chien, S. & Artmann, G.M. Temperature Transition of Human Hemoglobin at Body Temperature: Effects of Calcium. *Biophys. J.* **80**, 2622-2630 (2001).
70. Feng, S. & Sen, P.N. Percolation on Elastic Networks: New Exponent and Threshold. *Phys. Rev. B* **52**, 216-219 (1984).
71. Hubbard, A.T. *Encyclopedia of Surface and Colloid Science.* (Marcel Dekker, 2002).
72. Henriksen, J., Rowat, A.C. & Ipsen, J.H. Vesicle fluctuation analysis of the effects of sterols on membrane bending rigidity. *Eur. Biophys. J.* **33**, 732-741 (2004).
73. Evans, E. & Rawicz, W. Entropy-driven tension and bending elasticity in condensed-fluid membranes. *Phys. Rev. Lett.* **64**, 2094-2097 (1990).
74. Hagerstrand, H. & Isomaa, B. Lipid and protein composition of exovesicles released from human erythrocytes following treatment with amphiphiles. *Biochim Biophys Acta* **1190**, 409-415 (1994).
75. Tang, W. & Thorpe, M.F. Percolation of elastic networks under tension *Phys. Rev. B* **37**, 5539 (1988).
76. Bursac, P. *et al.* Cytoskeletal remodelling and slow dynamics in the living cell. *Nat. Mater.* **4**, 557-561 (2005).
77. Siegel, D. Partial purification and characterization of an actin-bundling protein, band 4.9, from human erythrocytes. *The Journal of Cell Biology* **100**, 775-785 (1985).
78. Marko, J.F. & Siggia, E.D. Stretching DNA. *Macromolecules* **28**, 8759-8770 (1995).
79. Evans, E. & Fung, Y.C. Improved measurements of the erythrocyte geometry. *Microvasc Res* **4**, 335-347 (1972).
80. Schmid-SchoNbein, H., Wells, R.O.E. & Goldstone, J. Influence of Deformability of Human Red Cells upon Blood Viscosity. *Circ. Res.* **25**, 131-143 (1969).
81. Mohandas, N., Clark, M.R., Jacobs, M.S. & Shohet, S.B. Analysis of factors regulating erythrocyte deformability. *Journal of Clinical Investigation* **66**, 563 (1980).
82. Bouchiat, C. *et al.* Estimating the persistence length of a worm-like chain molecule from force-extension measurements. *Biophys J* **76**, 409-413 (1999).
83. Wells, R. & Schmid-Schonbein, H. Red cell deformation and fluidity of concentrated cell suspensions. *Journal of Applied Physiology* **27**, 213-217 (1969).
84. Park, Y. *et al.* Refractive index maps and membrane dynamics of human red blood cells parasitized by Plasmodium falciparum. *Proc. Natl. Acad. Sci. U.S.A.* **105**, 13730 (2008).
85. Kilejian, A. Characterization of a Protein Correlated with the Production of Knob-Like Protrusions on Membranes of Erythrocytes Infected with *Plasmodium falciparum*. *Proc. Natl. Acad. Sci. U.S.A.* **76**, 4650-4653 (1979).
86. Sherman, I.W. Biochemistry of Plasmodium (malarial parasites). *Microbiological Reviews* **43**, 453 (1979).
87. Goldberg, D.E., Slater, A.F.G., Cerami, A. & Henderson, G.B. Hemoglobin Degradation in the Malaria Parasite *Plasmodium falciparum*: An Ordered Process in a Unique Organelle. *Proc. Natl. Acad. Sci. U.S.A.* **87**, 2931-2935 (1990).

88. Nash, G.B., O'Brien, E., Gordon-Smith, E.C. & Dormandy, J.A. Abnormalities in the mechanical properties of red blood cells caused by Plasmodium falciparum. *Blood* **74**, 855-861 (1989).
89. Cranston, H.A. *et al. Plasmodium falciparum* maturation abolishes physiologic red cell deformability. *Science* **223**, 400-403 (1984).
90. Paulitschke, M. & Nash, G.B. Membrane rigidity of red blood cells parasitized by different strains of Plasmodium falciparum. *J Lab Clin Med* **122**, 581-589 (1993).
91. Miller, L., Baruch, D., Marsh, K. & Doumbo, O. The pathogenic basis of malaria. *Nature* **415**, 673-679 (2002).
92. Gov, N.S. & Safran, S.A. Red Blood Cell Membrane Fluctuations and Shape Controlled by ATP-Induced Cytoskeletal Defects. *Biophys. J.* **88**, 1859 (2005).
93. Lawrence, C.L.L., Gov, N. & Brown, F.L.H. Nonequilibrium membrane fluctuations driven by active proteins. *J. Chem. Phys.* **124**, 074903 (2006).
94. Tilley, L., McFadden, G., Cowman, A. & Klonis, N. Illuminating Plasmodium falciparum-infected red blood cells. *Trends Parasitol.* (2007).
95. Lee, J.C.M. & Discher, D.E. Deformation-Enhanced Fluctuations in the Red Cell Skeleton with Theoretical Relations to Elasticity, Connectivity, and Spectrin Unfolding. *Biophys. J.* **81**, 3178-3192 (2001).
96. Minetti, M., Ceccarini, M., Di Stasi, A.M.M., Petrucci, T.C. & Marchesi, V.T. Spectrin Involvement in a 40ºC Structural Transition of the Red Blood Cell Membrane. *J. Cell. Biochem.* **30**, 361-370 (1986).
97. Da Silva, E. *et al.* The Plasmodium falciparum protein RESA interacts with the erythrocyte cytoskeleton and modifies erythrocyte thermal stability. *Mol. Biochem. Parasitol.* **66**, 59-69 (1994).
98. Oakley, M.S.M. *et al.* Molecular Factors and Biochemical Pathways Induced by Febrile Temperature in Intraerythrocytic Plasmodium falciparum Parasites?? *Infect. Immun.* **75**, 2012-2025 (2007).
99. Park, Y. *et al.* Metabolic remodeling of the human red blood cell membrane. *Proceedings of the National Academy of Sciences* **107**, 1289 (2010).
100. Mohandas, N. & Evans, E. Mechanical Properties of the Red Cell Membrane in Relation to Molecular Structure and Genetic Defects. *Annual Reviews in Biophysics and Biomolecular Structure* **23**, 787-818 (1994).
101. Zilker, A., Engelhardt, H. & Sackmann, E. Dynamic reflection interference contrast (RIC-) microscopy: a new method to study surface excitations of cells and to measure membrane bending elastic moduli. *J. Physique* **48**, 2139-2151 (1987).
102. Popescu, G., Park, Y.K., Dasari, R.R., Badizadegan, K. & Feld, M.S. Coherence properties of red blood cell membrane motions. *Phys. Rev. E* **76**, 31902 (2007).
103. Tuvia, S. *et al.* Cell membrane fluctuations are regulated by medium macroviscosity: Evidence for a metabolic driving force. *Proc. Natl. Acad. Sci. U. S. A.* **94**, 5045-5049 (1997).
104. Evans, J., Gratzer, W., Mohandas, N., Parker, K. & Sleep, J. Fluctuations of the Red Blood Cell Membrane: Relation to Mechanical Properties and Lack of ATP Dependence. *Biophys J* **94**, 4134 (2008).
105. Betz, T., Lenz, M., Joanny, J. & Sykes, C. ATP-dependent mechanics of red blood cells. *Proc. Natl. Acad. Sci. U. S. A.* **106**, 15312–15317 (2009).
106. Sheetz, M. & Singer, S. On the mechanism of ATP-induced shape changes in human erythrocyte membranes. I. The role of the spectrin complex. *Journal of Cell Biology* **73**, 638-646 (1977).

107. Parpart, A. & Hoffman, J. Flicker in erythrocytes. "vibratory movements in the cytoplasm"? . *Journal of Cellular and Comparative Physiology* **47**, 295-303 (1956).
108. Gov, N.S. Active elastic network: Cytoskeleton of the red blood cell. *Phys.Rev.E* **75**, 11921 (2007).
109. Li, J., Lykotrafitis, G., Dao, M. & Suresh, S. Cytoskeletal dynamics of human erythrocyte. *Proc. Natl. Acad. Sci. U. S. A.* **104**, 4937 (2007).
110. Zhang, R. & Brown, F. Cytoskeleton mediated effective elastic properties of model red blood cell membranes. *The Journal of Chemical Physics* **129**, 065101 (2008).
111. Auth, T., Safran, S. & Gov, N. Fluctuations of coupled fluid and solid membranes with application to red blood cells. *Physical Review E* **76**, 51910 (2007).
112. Mizuno, D., Tardin, C., Schmidt, C. & MacKintosh, F. Nonequilibrium Mechanics of Active Cytoskeletal Networks. *Science* **315**, 370 (2007).
113. Liu, F., Mizukami, H., Sarnaik, S. & Ostafin, A. Calcium-dependent human erythrocyte cytoskeleton stability analysis through atomic force microscopy. *Journal of Structural Biology* **150**, 200-210 (2005).
114. Muller, E. *et al.* Turnover of phosphomonoester groups and compartmentation of polyphosphoinositides in human erythrocytes. *Biochemical Journal* **235**, 775 (1986).
115. Patel, V. & Fairbanks, G. Spectrin phosphorylation and shape change of human erythrocyte ghosts. *Journal of Cell Biology* **88**, 430-440 (1981).
116. Agre, P. & Parker, J. *Red blood cell membranes: structure, function, clinical implications.* (CRC Press, 1989).
117. Manno, S., Takakuwa, Y. & Mohandas, N. Modulation of erythrocyte membrane mechanical function by protein 4.1 phosphorylation. *Journal of Biological Chemistry* **280**, 7581 (2005).
118. Beutler, E. *Williams hematology.* (McGraw-Hill New York, 1995).
119. Tchernia, G., Mohandas, N. & Shohet, S. Deficiency of skeletal membrane protein band 4.1 in homozygous hereditary elliptocytosis. Implications for erythrocyte membrane stability. *Journal of Clinical Investigation* **68**, 454 (1981).
120. Fred, M. & Pickens, M. Metabolic dependence of red cell deformability. *The Journal of Clinical Investigation* **48**, 795 (1969).
121. Park, Y.K., Popescu, G., Badizadegan, K., Dasari, R.R. & Feld, M.S. Diffraction phase and fluorescence microscopy. *Opt Express* **26**, 1271-1273 (2007).